# Recent advances on enhancing the multicarbon selectivity of nanostructured Cu-based catalysts

**Gustavsen, Kim Robert; Wang, Kaiying**

Department of Microsystems, University of South-Eastern Norway, Borre 3184, Norway.

# Recent Advances on Enhancing the Multicarbon Selectivity of Nanostructured Cu-based Catalysts

Kim R Gustavsen and Kaiying Wang*

*Department of Microsystems, University of South-Eastern Norway, Borre 3184, Norway.
Email: Kaiying.Wang@usn.no*

**Abstract:** Rapid development and affordability of renewable energy sources necessitates innovative energy storage technologies to compensate for their intermittency. Electrochemical reduction of $CO_2$ presents an attractive strategy for renewable energy storage, with considerable advancements in the recent years. Copper-based catalysts has spearheaded this progress due to its intrinsic ability to produce valuable multicarbon reaction products. However, Cu is inherently unselective, and considerable efforts are needed to achieve selective production of multicarbon reaction products on Cu-based catalysts. A multitude of factors affects the selectivity of the Cu-catalyst, such as, morphology, metal co-catalysts, and incorporation of oxidizing agents. In this review we have summarized the current progress and the most important strategies for tuning the selectivity towards multicarbon reaction products over nanostructured Cu-based catalysts.

**Keywords:** *Electrochemical $CO_2$ reduction, Multicarbon reaction products, Cu-based catalysts*

# Introduction

Rising level of $CO_2$ in the atmosphere is one of the biggest challenges we face in modern society. Despite the measures taken to decrease carbon emissions, the atmospheric $CO_2$ content exceeded 400 ppm in July 2015[1], and based on projection the atmospheric $CO_2$ concentration will be between 540 – 970 ppm at the end of the century depending on economic growth and fossil fuel usage [2, 3]. Transitioning from fossil fuel-based energy to renewable sources is the potential remedy needed to ensure a sustainable future. Unfortunately, renewable energy sources usually have a fluctuating power output, sometimes completely mismatching the energy demand. To address this issue, we need to develop innovative ways of energy storage. On top of that, this stored energy should be readily available for transportation. Utilizing renewable energy to convert $CO_2$ and water into fuels or other valuable chemicals are among the most attractive propositions. However, the reduction of $CO_2$ is an unfavourable chemical process where one electron reduction of $CO_2$ occurs at a thermodynamic potential of -1.90 V vs. SHE. An extensive amount of research has therefore been focused on developing suitable catalysts for the conversion of $CO_2$, but high Faradaic efficiencies (FE) at reasonable current densities has been achieved exclusively for two-electron reduction products like CO or HCOOH. The FE is defined as the ratio between the measured amounts of reaction product to the theoretical amount based on charge transferred in the electrochemical reaction, and is commonly used to evaluate the selectivity of a catalyst. Reduction to energy dense two-carbon ($C_2$) hydrocarbons and alcohols are highly desirable, but are harder to catalyse and require large overpotentials, leading to large energy loss during conversion. To date, copper is the only metal that possess the ability to produce $C_2+$ hydrocarbons and oxygenates at proper efficiencies [4]. The drawback is that Cu is inherently unselective and produces a wide range of reaction products, with $C_2$ products being the minor ones. In addition, considerable hydrogen evolution reaction (HER) takes place, lowering the $CO_2$ reduction efficiency. HER refers to the production of hydrogen through the electrolysis of water, which is in direct competition with $CO_2$ reduction. One way of steering the selectivity towards multicarbon products while simultaneously quenching HER is to increase the binding strength of *CO (the asterisk denotes a chemisorbed species) to promote C-C coupling [5]. Unfortunately, tuning the selectivity while simultaneously lowering the overpotential is challenging due to the linear scaling relations among the adsorption energies of the reaction intermediates [6]. For instance, increasing the binding strength of *CO will also increase the adsorption energy of *CHO. This means that one cannot tune the adsorption energy of one intermediate independently without affecting the associated activation barriers and binding of subsequent intermediates. Consequently, the rate-determining step will require a high overpotential [7]. Therefore, emphasis should be on developing a Cu catalyst capable of circumventing the linear scaling relations, for instance by utilizing dual active sites.

Several excellent reviews have been published on the topic of $CO_2$ reduction reaction ($CO_2RR$) related to Cu-based catalysts [8-14]. Among them, Cuenya et al. have partially tackled design of Cu based catalysts and the potential for multicarbon formation on a diverse selection of Cu and non-Cu catalysts [13]. However, a complete in-depth progress report on engineering nanostructured Cu-based catalysts to achieve selective multicarbon production is needed for the rapid development of $CO_2$ utilization. In this paper, we summarize and analyse various strategies for enhancing multicarbon selectivity. These strategies include controlling morphology in terms of its crystallographic properties, introduction of

additional metal sites and alloying, oxide-derived Cu and alternative oxidizer agents, utilization of metal organic frameworks (MOF), and optimizing the electrolyte in terms of cations and additives.

## Basic concepts and reaction pathways

Copper-based catalysts are unique since they can lead to a multitude of reaction products, including multicarbon products. Despite this advantage, the selective formation of one product is challenging due to the reaction products exhibiting very similar redox potentials (Table 1) [15]. Therefore, a thorough understanding and evaluation of the reaction pathways is necessary for developing a selective Cu catalyst. The reaction mechanisms for $CO_2$ reduction on Cu catalysts have been studied for a long time both by experimental and computational means. While the electrochemical reduction of $CO_2$ into multicarbon products is highly complex due to the amount of reaction intermediates, the rapid development of computational chemistry in combination with *in-situ* measurement techniques have broadened our understanding of the kinetic reaction pathways. However, performing full kinetic studies to outline all the potential reaction pathways towards multicarbon products with the inclusion of explicit factors such as, ions and solvent layers and adsorbate-adsorbate interaction are currently not practical due to the computational requirements [16].

The initial step of $CO_2$ reduction on a Cu (100) surface occurs first through physisorption of $CO_2$, which then proceeds to form chemisorbed $CO_2$. Formation of CO occurs through the protonation of *$CO_2^-$ to form COOH* followed by the dissociating of COOH* to form *CO and OH* [17]. Whereas formate is suggested to form through the *OCHO intermediate [18], or alternatively by a direct reaction of physisorbed $CO_2$ with a *H , which would make it a direct competitor with CO formation in the first electron step of $CO_2$ reduction [17]. Despite the fact that formic acid has shown to reduce to methanol at Sn and In [19, 20], the formation of formate/formic acid at Cu is considered as a dead end towards further reduction. In fact, adding formate and formic acid to the electrolyte yields no reaction products at Cu, except for minute quantities of methane from formic acid at very large overpotentials [21, 22]. On the other hand, *CO has been identified as a key intermediate for the subsequent reduction products, which becomes obvious when using a CO feedstock, resulting in a near identical product distribution for the main reaction products like $CH_4$ and $C_2H_4$, but with a near total quenching of HCOOH [23]. Following the formation of *CO, the protonation leads to either *CHO or *COH. The existence of one over the other has been debated, and depending on the coordination number of the active sites on the Cu surface they may coexist [24]. Reaction pathways for the major C1 products is relatively well established, and a general overview is outlined in figure 1. Both methane and the $C_2$ products share a common intermediate in *CHO/*COH where an additional protonation to *$CH_2O$ leads to methane formation and coupling with *CO to form *COCHO/*COCOH results in $C_2$ products [25]. Alternatively, the $C_2$ formation can occur through the dimerization of two adjacent *CO to form *COCO, which subsequently undergoes protonation to form *COCHO/*COCOH. Furthermore, factors such as crystal orientation and applied potential alter the reaction pathways. For instance, methane is the major product over Cu (111), whereas ethylene is favourable over Cu (100) surfaces [26]. This can be attributed in part to the higher binding energy of *CO on Cu (100) compared to Cu (111) [27], which opens an additional CO-CO coupling pathway on the Cu (100) surface at lower

potentials [28]. However, at more negative potentials the CHO* pathway becomes thermodynamically favourable on both Cu (100) and (111), resulting in the simultaneous formation of methane and ethylene. This is consistent with calculations where an increased potential have shown an increase in the kinetic barrier for *CO dimerization and a decrease in the kinetic barrier for *CHO formation through the Heyrovsky mechanism on Cu (100), as seen in figure 2 a and b, respectively [29].

While the separation of the $C_1$ and $C_2$ pathways are relatively well established, the post C-C coupling reaction mechanisms are debateable. After the initial C-C coupling there is a variety of suggested pathways towards the most common multicarbon products ethylene and ethanol. These suggested reaction mechanisms were integrated into a single scheme by Todorova et al. [30], and can be seen in figure 3. The suggested reaction pathways are based on the works of Bell and Head-Gordon (red) [28], Goddard et.al (pink) [31, 32], Janik and Asthagiri (blue) [33], and Calle-Vallejo and Koper (green) [34, 35], with brackets encompassing different tautomers of the intermediates. To tune the selectivity in favour of either ethanol or ethylene, we need to identify the selectivity-determining intermediate (SDI), the reaction step in which two reaction pathways separates. Perhaps most interesting is the proposition of *COCHO as the SDI by Bell and Head-Gordon, which proceeds to form either glyoxal in the ethanol pathway or *COCHOH in case of ethylene. It is predicted that glyoxal might be chemisorbed at the surface during reaction conditions where it is reduced to ethanol and acetaldehyde (CH$_3$*CHO*) at high and low potentials, respectively. Thus, the two pathways are divided at an early stage after the C-C coupling step. Moreover, the formation of glyoxal has experimentally been verified [36], and has shown to reduce primarily to ethanol with small quantities of acetaldehyde [37, 38]. Most notably, ethylene could not be detected for any of these cases, therefore it is unlikely that glyoxal and acetaldehyde leads to ethylene formation. Similar to glyoxal, acetaldehyde produces mainly ethanol over Cu [39], indicating that the pathways must indeed separate at an earlier step if acetaldehyde is a key intermediate for ethanol formation, like suggested by Calle-Vallejo and Koper. Bell and Head-Gordon also includes acetaldehyde in their scheme, eventually forming ethylene hydroxide (*CH$_2$CH$_2$OH) in the last step of ethanol formation. On the other hand, while Janik and Asthagiri following Bell and Head-Gordon's work includes ethylene hydroxide in the last reaction step, they suggest a lower activation barrier for ethylene formation (0.39 eV) than for ethanol formation (0.75 eV) over Cu (100). Moreover, they find that the barrier for breaking the O-C bond in ethylene oxide (CH$_2$CH$_2$O*) to form ethylene is rather high (1.01 eV) and is therefore more likely to form ethylene hydroxide with a barrier of 0.85 eV. This is contrary to Calle-Vallejo and Koper's suggestions, where the C-O bond of ethylene oxide is cleaved easily to form ethylene. In fact, experimental evidence supports this premise, with the reduction of ethylene oxide resulting in ethylene formation at potentials below that required for the reduction of CO [38]. Furthermore, Calle-Vallejo and Koper, like Bell and Head-Gordon, considers the formation of *CCO from *COCOH favourable. However, Goddard et.al insists that the formation of *COHCOH is more favourable with a barrier 0.67 eV lower than *CCO. They also argue that the bifurcation takes place at *CH*COH, with the formation of the ethylene intermediate *CCH* being more favourable than the ethanol intermediate *CHCHOH, with barriers of 0.61 eV and 1.05 eV, respectively.

4

In summary, the initial reaction mechanism to CO is relatively well understood. The main competitive $C_1$ products are $HCOO^-$ and $CH_4$. Whereas $HCOO^-$ could form through the direct reaction of $*H$ with physisorbed $CO_2$, there are also suggestions that it similar to $CH_4$ forms through the CHO/COH intermediate. Therefore, in order to maximize $C_2$ product selectivity the CO-CO coupling should be made favourable for the $C_1$ and $C_2$ pathways to bifurcate prior to the formation of CHO/COH. While separating the $C_1$ and $C_2$ reaction pathways from each other are rather clear-cut, the separation of the individual $C_2$ reaction pathways is vastly more complex. While we see great progress in the understanding of the $C_2$ reaction mechanisms in particular by DFT calculations, there is still not a clear consensus on the separation of the ethanol and ethylene pathways. We find the experimental detection and reduction of glyoxal to ethanol particularly interesting, and we strongly encourage similar approaches as it gives invaluable insights into determining the separation of the $C_2$ reaction product pathways when combined with DFT models.

## Enhancing the multicarbon selectivity

In the previous section, we established the fundamental aspects governing the reaction pathways and selectivity. We will proceed to delve into how this knowledge can be applied to develop novel strategies for improving the multicarbon selectivity of nanostructured Cu-based catalysts, primarily through enhancing the C-C coupling step. Common approaches to enhance multicarbon formation include strengthening the binding of CO and increasing the $*CO$ coverage. The destabilization of a certain intermediate is another route to further tune the selectivity of individual multicarbon products, like ethylene and ethanol. In this section we will look at most important properties governing the multicarbon selectivity of Cu-based catalysts. The reader should be aware that we in the following chapter designate a surface bound species with an asterisk in front of the intermediate without specifying the exact position of the bonds (unless stated in the reference). A summary of the various catalysts discussed in this section and the reaction conditions are listed in table 2.

### *Facet engineering and grain boundaries*

Altering the morphology of the Cu surface is a common strategy for controlling the product selectivity towards $C_2$ products. This includes facet engineering, creation of nanostructures, and formation of grain boundary rich surfaces. It is widely accepted that the product selectivity is heavily influenced by crystal orientation of the Cu surface. Most notably, the Cu(100) surface have a propensity for ethylene production, whereas the Cu(111) surface tends to favour methane formation [26]. Mechanistically this occurs due to the possibility of an additional CO-dimerization pathway exclusively for the Cu (100) surface at low reduction potentials. Thus, the $C_2H_4$ onset potential is considerably higher for Cu (111) as it requires the protonation of $*CO$ species [28, 40]. However, at high reduction potentials the coupling of $*CO$ and $*CHO$ becomes more favourable than CO-dimerization on Cu (100), thus resulting in a more similar product distribution between Cu (100) and Cu (111) [29, 41]. Stepped facets like Cu (211) is also more selective towards $C_2$ products compared to Cu (111) due to favourable kinetics for CO dimerization [16]. Therefore, creation of nanostructured Cu catalysts containing a large fraction of Cu (100) sites is a viable strategy towards $C_2$

product selectivity. For instance, nanocubes with Cu {100} terraces demonstrates the dependence of the selectivity on the facet, since they give rise to large areas of Cu {100} sites, favouring ethylene formation [42]. Interestingly, nanocubes exhibit high yield of ethylene in comparison to polycrystalline Cu (100) surfaces. This is due to a synergistic dual-facet mechanism at the interface of the {100} terrace sites and {110} edges favouring COH-CO coupling over CO dimerization. Protonation of adsorbed CO species into *COH occurs at the {110} edge and subsequent coupling with the bound CO intermediate at the {100} terrace eventually leads to ethylene formation [43]. In fact, this appears to be mutually valid for (110) and (111) steps on (100) terraces [26]. Furthermore, the ratio between terrace and edge sites are modified by altering the size of the nanocubes. For instance, Cu nanocubes with sizes of 24, 44, and 63 nm display a parabolic trend in ethylene FE, with the smallest nanocubes exhibiting significant HER due to the density of low-coordination sites, and the largest nanocubes attains a selectivity close to that of single crystal Cu (100), owing to the large terrace to edge ratio [44]. The 44 nm nanocubes were further evaluated against other nanostructured Cu catalysts in a gas-fed flow-cell configuration using alkaline electrolyte, attaining an ethylene FE of 57% at a current density of 300 mA/cm$^2$ (figure 4a) [45]. In comparison, the spherical nanocatalyst reaches a maximum FE of 31%, while the octahedral nanocatalyst exhibits suppression of ethylene formation in favour of methane (FE=51%). The selectivity towards methane occurs on the octahedral catalyst due to the presence of primarily (111) facets. On the other hand, the spherical nanocatalyst is more similar to the bulk copper reference, both in terms of its selectivity and the (100)/(111) peak ratio obtained by XRD (figure 4b). Controlled growth of preferential facets remains a difficult challenge; yet, innovative catalyst synthesis techniques, such as electrodeposition under $CO_2$ reduction (figure 4c) leads to an intermediate induced preferential growth of Cu (100) [46]. Initial DFT calculations indicate that at an equal coverage of 0.01 ML of surface bound $CO_2$ and its reduction intermediates (*COOH and *CO), the Cu (111) is more stable than Cu (100), meaning that the direct conversion of (111) into (100) is unlikely under reaction conditions (figure 4d). However, chemisorbed $CO_2$ and its reduction intermediates possess higher binding energy on Cu (100) relative to Cu (111) and Cu (211) resulting in a 0.33ML coverage, higher than the 0.01ML on Cu (111) (figure 4e). As a result, the surface energy of Cu (100) is lowered, making it more stable than Cu (111). Therefore, the preferential growth of Cu (100) occurs by electrodeposition under $CO_2$RR conditions. A 10 second deposition results in a doubling in size of the initial nanoparticle seeds from 10 to 20 nm. Simultaneous growth of nanoparticles and dendrites occurs when increasing the deposition time to 60 seconds. The catalyst (60s Cu-$CO_2$) exhibits a Cu (100) to Cu (111) ratio approximately 1.7 times larger than the reference catalyst deposited under HER conditions, while a $C_{2+}$ (includes C3 reaction products) FE of 90% at a partial current density of 520 mA/cm$^2$ is obtained in a flow cell configuration.

Besides surface orientation, presence of grain boundaries also enhances the $C_{2+}$ selectivity. In fact, quantification of grain boundaries shows a linear correlation between the density of grain boundaries and $C_{2+}$ selectivity for CO reduction [47]. Moreover, an increase in the number of grain boundaries can occur due to morphological changes during reaction conditions. For instance, the fragmentation of ~20 nm $Cu_2O$ nanoparticles into densely packed 2-4nm Cu nanoparticles over the course of 6 hours of $CO_2$RR increases the ethylene FE from 27% to 57.3% [48]. The enhanced ethylene efficiency is largely attributed to the large amount of grain boundaries resulting from the fragmentation, with the disordered surfaces at the grain

boundaries being the active sites [49]. These active sites display stronger CO binding, leading to an increased CO coverage and thus improving C-C coupling energetics. Furthermore, fragmentation only occurs for particles prepared using cysteamine as an immobilization agent, and only in the presence of $CO_2$ during reaction. These observations indicate that the restructuring relies on the interplay between the cysteamine and $CO_2$ reduction intermediates with the surface copper atoms to create defects. Similarly, a grain boundary rich Cu catalyst attaining an FE of 70% for ethylene and ethanol displayed a stronger absorption of *CO based on in-situ SEIRAS [50]. Additionally, the strain associated with an increasing density of grain boundaries play an important part in the favourable $C_{2+}$ selectivity. In fact, the grain boundary density is highly related to the microstrain. Annealing to reduce the quantity of grain boundaries also leads to a reduction in both strain and $C_{2+}$ FE [47]. However, annealing at moderate temperatures can retain most of the grain boundaries while still reducing the strain together with the $C_{2+}$ FE, indicating that the strain directly impacts the C-C coupling [49]. Furthermore, computational studies suggest that the strain increases the *CO coverage on all facets, while lowering the activation barrier for CO-dimerization on Cu (111) and reducing the reaction energy on Cu (211) [51]. Likewise, a monotonic increase in CO binding energy with surface roughness occurs for Cu catalysts roughened by exposure to a variety of plasma treatments (Ar, $O_2$, $N_2$) [52]. An increased stabilization of *OC-COH at newly formed active sites at the grain boundaries between Cu (100) and Cu (111) further enhances $C_{2+}$ product formation. Besides an over-all increase in $C_{2+}$ product formation observed for theses catalysts, there is a gradual improvement in $C_{2+}$ oxygenate selectivity as a function of surface roughness. Similarly, synthesis of a range of catalysts with different roughness factors (based on electrochemical double-layer capacitance measurements) display a linear relation between oxygenate FE and surface roughness for CO reduction (figure 4f) [53]. With the Cu nanoflower catalyst exhibiting a surface roughness factor of ~ 390 achieves nearly full selectivity towards $C_2$ oxygenates. A rise in local pH due to increased roughness can suppress HER and thereby enhance $C_2$ FE [54], although, in both cases the change in local PH was deemed too small to be significant.

In summary, Cu (100) appears preferential when optimizing the multicarbon selectivity. The creation of nanostructures gives rise to large surface areas, which is beneficial for achieving high geometric current densities. Furthermore, the selectivity is highly dependent on the size of the nanostructures, putting stringent demands on the fabrication processes. As such, we see that Cu nanocubes can combine both these aspects and seems like a decent starting point when considering further functionalization.


*Metallic tandem catalysts and alloys*

Integrating a second metal by alloying with Cu or as a cocatalyst in a tandem catalysis scheme is a viable strategy to improve $C_2$ selectivity. Tandem catalysts exploit a relatively high yield of CO on metals such as Ag, Au, and Zn. The CO works as a feedstock for the adjacent Cu sites, where the CO is further reduced to $C_2$ products. Additionally, alloying alters the binding strength of the reaction intermediates like *CO and *COOH. $CO_2$RR volcano plots gives binding energies for a variety of metals and are useful for predicting the effect of alloying, to selectively stabilize or destabilize reduction intermediates [5]. For instance, *HCCOH is assumed a common intermediate for ethylene and ethanol that proceeds either towards *CCH for $C_2H_4$ or *HCCHOH for $C_2H_5OH$, depending on the relative stabilities of the surface

intermediates (figure 5a) [32]. Therefore, introducing appropriate amounts of metals that bind carbon weaker than Cu can disrupt the ethylene pathway on Cu (111) in favour of ethanol. This concept was used to develop a $Ag_{0.14}/Cu_{0.86}$ alloy catalyst, reaching a FE of 41% for ethanol with a current density of 250 mA/cm$^2$ at -0.67V vs. RHE in a flow cell reactor (figure 5b) [55]. Furthermore, controlling the Ag-Cu ratio affects the ethanol vs. ethylene selectivity. In another example, a Ag-Cu wire catalyst containing 6% Ag displays a FE of 60% for ethylene and 25% for ethanol at a current density of ~ 300 mA/cm$^2$ [56]. It was postulated that the enhanced $C_2$ product formation occurs due to the stabilized Cu(I) oxides, owing to Ag incorporation. In comparison, at equal potentials, the Cu wire catalyst obtained an ethylene FE of 40% and half the partial current density. While both Cu(I) and Cu(II) oxides are present in the Cu wire reference, only Cu(I) is detected for the Ag-Cu wire. This result contradicts previous reports that Ag renders Cu resistant to oxidation [57]. However, it can be argued that this conclusion was drawn primarily based on XPS data, in which it would be impossible to differentiate between $Cu_2O$ and Cu. Alternatively, alloying with Au can enhance ethanol formation. For instance, an ethanol FE of 29% and a relative suppression in ethylene formation occurs for Au-Cu nanoparticles embedded in Cu submicrocone arrays [58]. DFT calculations suggests that the $CuAu_3$ surface possess a lower activation ability for the *CH$_2$CHO intermediate compared to Cu, resulting in shorter C-O bond lengths that are harder to break, thus favouring ethanol formation. Furthermore, the $CuAu_3$ retains a lower energy barrier for ethanol formation and a higher ethylene energy barrier compared to Cu (100). This result is consistent even when considering the alternate ethanol pathway through the concerted reaction of water molecules with *CCH to form*CHCHOH [59]. Similarly, alloying Cu with Zn enhances ethanol formation, with an ethanol FE of 46.6% being obtained by adjusting the Zn content in a porous Zn-Cu catalyst [60]. Moreover, increasing the Zn content leads to an increase in ethanol FE and reduction in HER activity. Interestingly, the highest ethanol FE is observed when the Zn content surpasses that of Cu ($Cu_5Zn_8$). More specifically, the HER suppression occurs owing to a higher *CO coverage due to the larger amount of CO produced by the Zn sites, which blocks proton reduction. Furthermore, calculations of the Gibbs free energy of hydrogen ($\Delta G_{H*}$) reveals a drastic weakening of *H binding, from 0.19 eV for pure Cu to 0.66 eV for the $Cu_5Zn_8$ catalyst.

Another approach is to incorporate metals as a cocatalyst with segregated metallic phases, providing a high amount of reaction intermediates such as *CO while leaving the Cu sites unaffected. For instance, a bimetallic Ag-Cu foam exhibits negligible ethanol formation, but thermal oxidation at 200 °C enables a shift in product selectivity from ethylene to ethanol (FE=33.7%). More specifically, the $Ag_2O$ is not thermally stable above 180°C, and the thermal annealing at 200°C therefore leads to oxidation of the Cu [61]. Since Ag binds *CO relatively weaker than Cu, it can generate a large flux of *CO which can be subsequently transported to adjacent Cu sites by surface diffusion or readsorption (figure 5c) to undergo C-C coupling [62]. While the increased amount of chemisorbed CO leads to favourable C-C coupling energetics [63], the further reduction into ethanol or ethylene is determined by the stability of their respective intermediates [32]. Operando Raman spectroscopy reveal a larger concentration of chemisorbed CO for the Ag-Cu foam compared to pure Cu as function of applied potential (figure 5d). In addition, the maximum integrated peak intensity is shifted approximately -100 mV for the as-deposited Ag-Cu foam, whereas thermal annealing results in an additional shift of -100 mV. The indicated improvement in stability and

coverage of *CO is beneficial for $C_2$ formation. In contrast, a Ag-Cu nanodimer catalyst results in mainly ethylene production with small amounts of ethanol (FE<5%) [63]. Optimizing the ratio of Ag and Cu in the nanodimers leads to a significant 3.4-fold increase in ethylene FE and a 2-fold increase in the partial current density for $CO_2$ reduction compared to the pure Cu nanoparticles (figure 5e). The nanodimers consist of segregated pure metallic Cu and Ag phases where the Ag provides a high abundance of *CO in the same manner as for the above-mentioned catalyst. However, the intermediate binding energies is unchanged for the copper particles. Consequently, ethylene remains the primary $C_2$ product even after the introduction of Ag, but the formation significantly increases due to the higher abundance of *CO. A similar tandem catalysis concept is observed for Au nanoparticles on a Cu foil where a local increase in CO concentration exceeding the solubility limit gives enhanced $C_{2+}$ product formation [64]. Furthermore, the $C_{2+}$/C1 ratio is largest for lower overpotentials where C-C coupling is more favourable than C1 formation. Comparing the Au/Cu tandem catalyst to the Cu foil indicates no difference in C1 production, meaning that the improved $C_{2+}$ product formation can be attributed to improved C-C coupling kinetics as opposed to C1 suppression. Moreover, the transfer of *CO from Au to Cu sites via surface diffusion (spillover) is thermodynamically favourable and is postulated as being responsible for the enhanced activity [65]. Likewise, the spillover phenomenon enables an ethanol FE of 29.1% at a partial current density of -8.2 mA/cm$^2$ for an oxide derived phase segregated $Cu_4Zn$ catalyst. The suggested pathway involves the surface diffusion of CO followed by a subsequent insertion into the bond between *$CH_2$ and the Cu surface to form $COCH_2$, which proceeds to form acetaldehyde before reducing to ethanol. Therefore, further increasing the Zn content results in less Cu sites capable of forming C1 intermediates (*$CH_2$) and consequently reduced ethanol formation [66].

In conclusion, alloying is a successful strategy for destabilizing intermediates, effectively disrupting either the ethanol or ethylene pathway, and thereby altering the selectivity between the two. It is especially the CO-producing metals that are successfully integrated with Cu, owing to their weaker binding strength of carbon. In fact, they can alter intermediate binding energies, or alternatively provide an abundant amount of CO to be transferred to Cu sites for further reaction when in a phase segregated configuration.

*Influence of oxidizing agent*

Oxygen-derived (OD) Cu catalysts shows considerable multicarbon selectivity compared to its metallic counterpart, which is believed to arise from the existence of $Cu^+$ sites. However, $Cu^+$ sites themselves have proven to deteriorate the catalytic performance and have a higher activation barrier for both $CO_2$ activation and CO-dimerization (figure 6a). Instead, the combination of metallic $Cu^0$ and $Cu^+$ sites synergizes to effectively lower the energy barrier for CO dimerization by imposing opposite charges on the carbon atom of the adsorbed *CO intermediates (figure 6a) [67]. Therefore, subsurface oxides present during reaction conditions are often proposed as responsible for this enhanced $C_{2+}$ selectivity [68]. But then again, existence of oxides in the surface layers of the copper catalyst during reduction potentials has been highly debated. In fact, DFT calculations have proven that subsurface oxide is less stable in the subsurface than on the surface. An exception is in the deeper layers where it could potentially be stable for a longer period, but it would not affect $CO_2$ absorption [69]. Isotope labelling using $O^{18}$ have also demonstrated that

OD Cu retains < 1% of its original oxide during $CO_2RR$ (figure 6b). An oxygen induced surface reconstruction is also unlikely to stabilize the oxides due to the significant amount of undercoordinated surface atoms, which would accelerate oxygen diffusion to the surface [70]. The formation of a 1-2 nm amorphous layer at the surface of copper nanoparticles able to stabilize subsurface oxygen have been observed using quasi in situ TEM (figure 6c) and PAS. In fact, neither a change in oxygen content nor distribution could be detected after 1 hour at reduction potentials of -1.15V vs. RHE [71]. In situ surface-enhanced infrared absorption spectroscopy (SEIRAS) has given direct insight into function of oxidation state on the $C_2$ selectivity, since it can detect adsorbed intermediate species [72]. Notably from the SEIRAS spectra it was observed that the atop-adsorbed CO intermediate tends to form on catalysts with primarily $Cu^+$ sites. For its metallic $Cu^0$ counterpart the formation of the residual bridge-adsorbed CO (CO bound to two Cu atoms) is dominant, which is considered inert to further reduction [73], and consequently a quenching of hydrocarbon production is detected. Coexistence of both *CO intermediates are detected for the catalyst containing a mixture of $Cu^0$ and $Cu^+$ oxidation states (figure 6d). Furthermore, a drastic increase in $C_2H_4$ selectivity (FE ~40%) occurs when having a mixture of $Cu^0$ and $Cu^+$ sites (figure 6e), consistent with computational studies on mixed oxidation state catalysts [67]. Innovative methods such as plasma oxidation gives precise control over the oxidation process. In fact, a plasma treated Cu foil reach a $C_2H_4$ FE of 60% by optimizing the plasma exposure time and power [74]. Furthermore, the onset potential is drastically reduced from -0.85V to -0.5V vs. RHE with the catalyst being stable for 5 hours during $CO_2RR$. A rise in local PH due to the roughened surface resulting from the plasma treatment could potentially quench the protonation of adsorbed *CO intermediates required for production of methane, whilst not affecting CO-dimerization, resulting in ethylene production [75]. However, increasing the plasma exposure time and power over a certain threshold results in a decline in $C_2H_4$ efficiency even as the surface roughness kept increasing. Moreover, surface roughness cannot explain the significantly reduced onset potential. In a similar fashion, $O_2$ plasma treated copper nanocubes show slightly improved $C_{2+}$ activity despite the fact it results in less well-defined Cu (100) facets, which typically have a propensity for ethylene production [76]. On the other hand, recent utilization of Ar+ plasma have demonstrated a similar selectivity behavior as $O_2$ plasma treated copper. Surface roughness alone was deemed fully responsible for the improved activity with no correlation to the oxidation state [52]. It should be noted that compared to the aforementioned study the roughness values were roughly 10 times lower for the catalyst with best performance. Nevertheless, plasma oxidation is generally a very promising concept as it allows for high control over the formation of oxides as opposed to more traditional oxidation methods like various thermal treatments.

Stabilization of $Cu^+$ sites at the copper surface are possible by incorporating alternative oxidizer agents. For instance, utilizing small amounts of boron as a dopant enables stable reduction of $CO_2$ into ethylene (FE ~50%) exceeding 40 hours of operation (figure 7a) [77]. This is rather significant as the OD-Cu and Cu reference catalyst deactivated after 12 and 6 hours, respectively. Boron incorporated into the catalyst increases the binding energy of *CO on the copper surface due to exhibiting a higher overlap amongst binding states between $C_{2P}$ and $Cu_{3d}$, thus favoring CO dimerization. Stronger binding of *CO leads to higher coverages, which lowers the energy barrier for CO-dimerization [78]. Through averaging the oxidations state over the active surface, the FE for $C_2$ products is maximized at ~79% for an average

oxidation state of 0.35. As opposed to oxygen atoms, boron is more stable in the subsurface octahedral sites than on the surface or bridge adsorption sites, and diffusion into the bulk is unlikely as it is kinetically and thermodynamically unfavorable [79]. Indeed, boron appears as a viable option for increasing the $C_2$ selectivity and have also successfully promoted $C_2$ production in OD-derived Cu catalysts (FE 48.2%) [80]. Similarly, subsurface Sulphur atoms alter the electronic structure of adjacent atoms and effectively strengthens the binding energy of *CO. Also, Cu chalcogenide nanocrystals possess a high degree of self-doping, which allows for precise control of the density of surface vacancies [81]. Controlled introduction of surface vacancies in nanoparticles with an outer metallic Cu(0) shell and $Cu_2S$ core (figure 7b) narrows the product distribution in favor of ethanol and propanol [82]. Vacancies in the pristine copper surface increases the energy barrier towards the ethylene pathway (*$C_2H_3O$ -> *O + $C_2H_4$) and rise further for the vacancy rich core shell nanoparticles. Meanwhile, the energy barrier for the ethanol pathway (*$C_2H_3O$ -> *$C_2H_4O$) stays relatively unchanged. This is of course based on the assumption that ethylene and ethanol share a common intermediate in *$C_2H_3O$ [83]. Compared to pristine copper, addition of Sulphur results in a shift from $C_2H_4$ to ethanol and propanol formation (figure 7b). Adding Cu vacancies further enhances the ethanol and propanol selectivity and a $C_{2+}$ alcohol FE of ~32% is attainable at a partial current density of 126 mA/cm$^2$ in a flow cell configuration. Functionalization of copper catalysts using halogens is a promising method yielding high selectivity towards $C_{2+}$ products. In particular, fluorine-modified Cu (F-Cu) is capable of delivering incredible current densities of 1.6 A/cm$^2$ at $C_{2+}$ FE's of 80% in an optimized flow cell configuration [84]. DFT calculations suggests that the route towards $C_2$ products proceeds through the protonation of *CO to *CHO followed by a subsequent coupling of *CHO to *OCHCHO as opposed to CO-dimerization. Interestingly, they found the dimerization of *CHO to be more favorable than CO-dimerization for both Cu(111) and F-Cu(111). Previously, this pathway has been assumed to primarily occur on stepped Cu (211) facets [85]. In-situ electrochemical attenuated total reflection Fourier-transform infrared spectroscopy (ATR-FTIRS) confirmed the presence of surface bound CO in the range of -0.1 to -0.3V vs. RHE at the F-Cu catalyst (figure 7c). Furthermore, the surface bound CHO predicted as a key intermediate is detectable from -0.4V vs. RHE and onwards. In comparison, *CO is not detected prior to -0.4V vs. RHE for the Cu catalyst, and CHO does not exist insufficiently high concentrations that would allow for detection (figure 7d). Besides Fluorine, various halogens were incorporated into the Cu surface resulting in enhanced $C_{2+}$ FE (figure 7e). Interestingly, the $C_{2+}$ FE increases and the $C_2H_4$ onset potential decreases in ascending order of halogen electronegativity (figure 7e inset). Larger electronegativity gives rise to a higher amount of Cu$^+$ sites, resulting in enhanced CO adsorption as evident from ATR-FTIRS spectra (figure 7c-d). Additionally, an increase in electronegativity might promote $H_2O$ dissociation, and in the case of Fluorine, the dissociation of $H_2O$ no longer becomes the rate-determining step. This is likely to occur due to non-covalent Coulomb interactions that results in the formation of $F^{\delta-}$-hydrated cation ($K^+(H_2O)_n$) networks in the double layer, similarly to Sulphur-modified indium catalysts [86].

While offering a relatively simple and effective way to steer the selectivity from methane to ethylene, the exact reaction mechanism on OD Cu is still being debated. We also see that the stability of the OD Cu catalysts are still rather poor. However, utilizing alternative oxidizer agents like Boron achieves superior stability, indicating that discovering more oxidizers besides oxygen that can attain a similar selectivity trend while offering prolonged stability is a promising concept. We believe that computational

models in combination with precise doping methods such as ion implantation offers tremendous potential and will likely become an emerging field for further functionalizing Cu catalysts.


*Metal organic frameworks (MOF)*

The use of metal organic frameworks (MOF) has become a research hotspot due to its ability to increase the coverage of the *CO intermediate without modulating the electronic structure of the Cu sites, and therefore avoiding the scaling relations. This property enhances the C-C coupling by generating a large abundance of CO that subsequently transfers to the Cu sites through the spillover effect. While this also occurs for bimetallic catalysts, their surface loading capacity is severely limited due to the formation of alloys that tends to alter intermediate binding energies on the Cu sites. Furthermore, MOFs allows for high surface area with controllable pore size, resulting in a more reliable way to preferentially tune the selectivity [87]. For instance, the molecular complex 5,10,15,20-tetraphenyl-21H,23H-porphine iron(III) chloride (FeTPP[Cl]) immobilized on a Cu surface steers the selectivity towards ethanol by operating as a $CO_2$ to CO converter [88]. The ratio of ethanol to ethylene formation surpasses 1 for the FeTPP[Cl]/Cu catalyst, approximately double the ratio of the Cu reference catalyst (figure 8a). Increased surface coverages of chemisorbed CO led to an increase in both ethanol to ethylene ratio and total $C_{2+}$ FE. The optimal surface coverage was near 1, where the surface coverage is defined as the surface ratio of additional *CO on a $3 \times 3$ Cu(111) surface. In comparison, the previously mentioned Au/Cu bimetallic catalyst exhibits an analogous ratio of 0.02 [64]. Notably, the ethanol formation declines when the surface coverage exceeds the threshold value due to a limitation of available Cu sites. Likewise, $Cu/Cu_2O$ nanoparticles loaded on graphene-based N-doped carbon (GNC) nanosheets derived from zeolitic imidazolate framework-L (ZIF-L) can boost ethanol formation [89]. In this experiment, Cu was incorporated into vertically grown ZIF-L on graphene oxide (GO) through a precursor, followed by a carbonization of the catalyst for 2 hours at 1000°C in nitrogen atmosphere to yield the Cu-GNC catalyst. The pyrolyzed ZIF-L itself exhibits poor ethanol selectivity with a FE of 8.64%, however; incorporation of Cu into the ZIF-L grown at GO increases the ethanol FE to 40.18%, whereas the Cu-GNC catalyst further increases the ethanol FE to 70.52% with a current density of 10.4 mA/cm$^2$ at -0.87V vs. RHE (figure 8b). The vastly improved activity was attributed towards the synergetic effects of large number of defects in the N-doped porous carbon, consecutive conductive network, $CO_2$ diffusion channels, and overall larger fraction of active sites. In addition, the stabilization of large amount of Cu(I) (70.58%) sites is likely to promote *CO dimerization. In gas-phase $CO_2$ reduction, a $Zr_{12}$-MOF functionalized with Cu and Cs, where the Cu is supported at the deprotonated $[Zr_{12}O_8(\mu_3\text{-O}^-)_8(\mu_2\text{-O}^-)_6(carboxylate)_{18}]^{14-}$ SBUs display nearly full selectivity towards ethanol in a high pressure reactor [90]. The turnover number (TON) reached 490 at a pressure of 2 MPa at 100°C, where the TON is defined as the number of moles of $CO_2$ converted into ethanol per mole of copper. Moreover, increasing the pressure to 35MPa while decreasing the temperature to 80°C leads to a TON of 4080.

HKUST-1 ($C_{18}H_6Cu_3O_{12}$, $Cu_3(btc)_2 \cdot xH_2O$, btc = benzene-1,3,5-tricarboxylate) is perhaps the most studied MOF due to its high $CO_2$ uptake, high surface area and large pore volume [91]. Structurally the HKUST-1 consists of Cu dimers connected by four benzene-1,3,5-tricarboxylate linker molecules in a

paddlewheel unit (figure 8c). As a catalyst for $CO_2$ reduction the HKUST-1 in its pristine produces primarily $CH_4$ while also exhibiting substantial HER activity [92]. However, controlled calcination allows for the sequential detachment of the carboxylic moieties, promoting undercoordinated Cu sites, resulting in an asymmetric motif [93]. Pre-treating the as-prepared HKUST-1 at 250°C for 3h leads to a 3-fold increase in $C_2H_4$ FE from 15% to 45%, while simultaneously decreasing the Cu-Cu coordination number from 11.3 to 9.5 (figure 8d). More specifically, the isothermal pre-treatment enables altering of the electronic configuration of Cu in a controlled manner to steer the selectivity towards $C_{2+}$ products while retaining the structural integrity of the HKUST-1 frame. HKUST-1 can also be used as a precursor for synthesis of OD Cu/C catalysts by carbonization processes [94]. Following carbonization for 6 hours at 1000°C, the Cu-based HKUST-1 catalyst exhibits an ethanol onset potential of -0.1V vs. RHE with a FE of 24%, which further increases to 34.8% when increasing the potential to -0.5V vs. RHE. The high selectivity towards ethanol arises from the synergistic effect of increased $Cu_2O$ content, pore diameter, and appropriate particle size. Comparatively, carbonization at 1100°C severely reduced the $CO_2$ reduction activity due to a reduction in pore size and agglomeration of the Cu nanoparticles, resulting in larger particle size and consequently less $Cu_2O$ content. Increased ethanol selectivity is also observed for MOF mixtures of Cu-based HKUST-1 and Bi-based CAU-17 [Bi(BTC)(H2O)] [95]. At a Bi content of 12%, the ethanol FE reaches 28.3% at a current density of 20 $mA/cm^2$. It is postulated that the increase in ethanol selectivity occurs due to the high formation of $HCOO^-$ intermediates at the Bi sites, which subsequently transfers to the Cu sites for further reduction towards ethanol. However, is it generally well established that while $HCOO^-$ reduces to methanol on Sn and In [19, 20], it does not reduce further on Cu sites [21, 22], making the suggested mechanism unlikely. Instead, it is possible that an alternative mechanism proceeding through $HCOO^-$ occurs due to synergy between CAU-17 and HKUST-1.

The integration of MOFs into the catalyst design for $CO_2$ reduction is an emerging method, which analogous to bimetallic catalysts can significantly enhance the CO coverage. Moreover, the MOF-based catalysts offer more freedom for controlling the morphology in terms of surface area and pore size as it does not suffer from the loading constraints as seen for the bimetallic systems. However, employing MOFs to boost multicarbon formation is a relatively new concept and the synthesis methods are rather complex. Therefore, a limited number of studies has been conducted in this area, and while the initial findings is promising, more research is required to fully assess the potential.

*Electrolyte and process conditions*

The formation of $C_{2+}$ products are optimized through process conditions such as cation type, concentration, pH, and additives. Experimental and theoretical studies show a clear correlation between the selectivity and electrolyte cation size. In particular, ethylene, ethanol, and $HCOO^-$ formation are affected by the cation size, where an increase in size results in an increased partial current density (figure 9a) [37]. DFT calculations suggests that a dipole field created by hydrated cations in the outer Helmholtz plane decreases the energy required for both the chemisorption of $CO_2$ and the C-C coupling for the formation of ethylene and ethanol intermediates *OCCO and *OCCHO. Furthermore, larger hydrated cations are favoured over smaller cations in the outer Helmholtz plane, resulting in larger coverage. A similar dependence on cation size has been observed for various Cu-based catalysts when tested in

electrolyte containing $Cs^+$ and $K^+$ cations [96]. The partial current of $H_2$ and $CH_4$ are unaffected, whereas partial currents for ethanol and ethylene increases with an increase in cation size. Altering the concentration of the electrolyte further influences the selectivity of the catalyst. For instance, ethylene is the major product in a 0.1M $KHCO_3$ electrolyte, however, increasing the concentration leads to an increase in methane formation, eventually making it the dominant reaction product at a concentration of 0.5M of $KHCO_3$ [97].

Microkinetic modelling of a Cu (211) surface indicates that $C_2$ product formation is favoured in more alkaline conditions (pH=13). Furthermore, for $C_2$ formation at low overpotentials the first proton-electron transfer to *OCCO is rate limiting, whereas the *CO coverage is limiting at high overpotentials. Therefore, at high overpotentials in alkaline conditions a decrease in $C_2$ product selectivity occurs due to a decrease in *CO coverage because of the competing C1 pathways [98]. In general, $CO_2$ reduction can be challenging under alkaline conditions due to the rapid reaction of dissolved $CO_2$ to form carbonates. On the other hand, using CO as the reactant instead of $CO_2$ allows for the use of alkaline electrolyte, enhancing the $C_{2+}$ product formation [99]. CO reduction in 0.1M KOH reveals that the rate determining steps of the $C_{2+}$ pathways are pH independent on an absolute potential scale, whereas the C1 formation is pH dependent. In effect, alkaline conditions reduces the overpotentials for $C_{2+}$ formation on an RHE scale due to favourable C-C energetics [100]. Reduction of $CO_2$ in alkaline electrolyte is possible by utilizing a gas diffusion layer in close approximation to the catalyst to enable the diffusion of $CO_2$ to the catalyst surface before it can react with the solution. This concept allows for higher concentrations of KOH solutions. In fact, the effect on the $C_{2+}$ formation is elevated for increasing concentrations of KOH, leading to a reduction in onset potential for $C_2H_4$, being as low as -0.165V vs. RHE in 10M KOH electrolyte. Furthermore, at 10 M concentration the onset potential for $C_2H_4$ and CO is nearly identical, which coupled with a drastically reduced tafel slope for ethylene (figure 9b) allows for an ethylene FE of 70% at a potential of -0.55V vs. RHE. [101].

Using organic additives in the electrolyte is another way to increase selectivity towards $C_{2+}$ products. Nearly 80% FE for $C_{2+}$ products has been obtained for a polycrystalline Cu catalyst using N-substituted pyridinium additives [102]. Post reduction characterization reveals that an organic thin film was deposited onto the Cu surface and a similar selectivity profile is attained when using this catalyst in a fresh electrolyte without additives. The pyridinium additives increases the $C_{2+}$ selectivity by suppresses methane and hydrogen formation but does not directly affect the $C_{2+}$ formation rate. Unfortunately, while ethylene is the major product, the selectivity and formation rate is still rather low, with a FE of ~40% at a partial current density of approximately 0.5 $mA/cm^2$. To build on this concept, new functional molecules were developed to improve the selectivity and formation rate of ethylene. A range of N-arylpyridinium precursors were electrodeposited onto a gas diffusion layer with a Cu layer, forming a mix of N-aryl-substituted tetrahydro-bipyridines through the electro-dimerization process. [103]. The ethylene FE as a function of the Bader charge of the N atoms reveals a volcano trend. Furthermore, an increase in atop adsorbed CO at the expense of bridge adsorbed CO is observed for increasing Bader charge of the N atoms, resulting in a similar volcano curve when plotting the FE against the ratio of $CO_{atop}$ to $CO_{bridge}$ (Figure 9c). CO adsorption in the atop configuration is enhanced due to the electron density transfer from the tetrahydro-bipyridine to the *CO, facilitated by the nearby water molecules. Based on these

observations, a N-aryl-dihydropyridine-based oligomer formed during electrodeposition was synthesized to increase the number of nitrogen sites to stabilize a larger amount of *CO intermediates, leading to a 72% FE for ethylene at a partial current density of 230 mA/cm$^2$ in 0.1M KHCO$_3$ using a flow cell configuration (figure 9d). Molecular additives such as N,N'-ethylene-phenanthrolinium dibromide (1-Br$_2$) is able to generate and stabilizing nanostructures through corrosion and subsequent formation of an organic film on polycrystalline Cu by an electro-dimerization process (figure 9e) [104]. Moreover, the formation of an organic film inhibits HER, leading to a five-fold decrease in hydrogen current density in comparison to a polycrystalline Cu catalyst, while stabilizing the nanostructures for over 40 hours of CO$_2$RR. Nearly 70% FE for C$_{2+}$ products is achieved using the 1-Br$_2$ additive, whereas other counter anions show a similar selectivity trend, but at reduced ethylene FE and currents. Interestingly, nanostructuring does not occur when using 1-Cl$_2$ due to the inability of Cl- to corrode the Cu surface, but HER is still drastically reduced compared to the pure Cu electrode in favour of ethylene. This indicates that the electrodeposited organic film plays an important role in enhancing the C$_{2+}$ formation, even in the absence of nanostructures. Utilizing ethylenediaminetetraacetic acid (EDTA) as an additive in combination with anodic pre-treatment of the Cu electrode can increase the stability of the catalyst. Moreover, the stability increases with higher concentrations of EDTA, leading to an ethylene retention rate of 91% after 20h of operation for a polycrystalline Cu at concentrations of 25μM [105]. The EDTA acts as a metal ion scavenger, removing minute metallic impurities originating from the electrolyte such as Zn, Sn, and Pb. Additionally, EDTA is suggested to increase the CO$_2$ concentration near the catalyst surface due to a local pH effect analogous to the size effect observed for large cations [106].

In summary, we note that the type of cation has high impact on the selectivity. Although, in most cases we observe the use of KHCO$_3$, which is beneficial for comparing catalysts between different systems. Clearly, alkaline electrolytes such as KOH is superior in terms of favouring C-C coupling but puts further constraints on the experimental setup and catalyst preparation, such as the requirement of GDEs. Furthermore, we see the development in terms of additives to be a promising alternative method for tuning the selectivity, proving that optimization of process conditions in combination with catalyst design is a prerequisite for obtaining a highly selective reduction process.

## Summary and outlook

We have reviewed the recent progress and strategies for enhancing the activity and multicarbon selectivity of Cu-based catalysts. The design of highly selective catalysts requires a fundamental understanding of the underlying reaction mechanisms on Cu surfaces. The advancement of computational chemistry in combination with in-situ measurement techniques has led to the identification of key intermediates and reaction pathways for the major multicarbon reaction products (ethylene and ethanol). Generally, from a reaction mechanism point of view the multicarbon selectivity can be enhanced by fulfilling the following principles – i) strengthening of CO binding energy, ii) increased coverages of CO. Both factors will favour C-C coupling and are often intertwined, since strengthening the CO binding energy often leads to higher coverages. However, we also see that they can be attained separately. For instance, we highlighted how the loading of CO selective metals such as Au and Ag provides an abundance CO to be further reduced by the Cu sites, while at same time leaving the binding energy of Cu unaffected.

This synergy between different active sites enables the oxidized matrix to be so effective. The fine tuning of the oxidation state by utilizing elements more stable than oxygen is a prime example this. In most of these cases the incorporation of the oxidizer agent is accomplished through wet chemical synthesis methods. We believe that doping by means ion implantation should be explored as it can further expand on the use of alternative oxidizing agents, by giving precise control over the dosage, while also being adaptable for a wide range of elements. It would therefore be a powerful method if used in conjunction with theoretical models and DFT calculations, as it could give a doping concentration matching that of the value derived from models to predict the most favourable C-C coupling energetics. We also observe that the use of MOFs is an emerging trend capable of increasing the CO coverage analogous to the phase separated bimetallic catalysts. A clear advantage with MOF-based catalysts is the high control over morphological properties like pore size and the absence of stringent loading constraints as seen for the phase-separated bimetallic catalysts to avoid alloy formation. Furthermore, we have elaborated on how external settings such as the reaction conditions can have a tremendous impact on the performance of the catalysts. We find the development of additives a promising route towards not only optimizing the reaction process, but also alter the catalyst properties in-situ. However, the optimization of process conditions also further diversifies the experimental setups used to evaluate catalysts. It can therefore be challenging to gauge the activity and selectivity independently of the experimental setups. Ideally, we would like to see a higher level of standardization, as it would be beneficial for future research and the development of electrochemical $CO_2$ reduction catalysts.

## Conflict of interest

The authors declare no conflict of interest.

## Acknowledgments

## References

1.  P. Tans and R. Keeling, *Journal*, 2015.
2.  J. E. T. Houghton, Y. Ding, D. Griggs, M. Noguer, P. van der Linden, X. Dai, M. Maskell and C. Johnson, *Climate Change 2001: The Scientific Basis*, 2001.
3.  J. T. Feaster, C. Shi, E. R. Cave, T. Hatsukade, D. N. Abram, K. P. Kuhl, C. Hahn, J. K. Nørskov and T. F. Jaramillo, *ACS Catalysis*, 2017, **7**, 4822-4827.
4.  Y. Hori, H. Wakebe, T. Tsukamoto and O. Koga, *Electrochimica Acta*, 1994, **39**, 1833-1839.
5.  X. Liu, J. Xiao, H. Peng, X. Hong, K. Chan and J. K. Nørskov, *Nature Communications*, 2017, **8**, 15438.
6.  C. Shi, H. A. Hansen, A. C. Lausche and J. K. Nørskov, *Physical Chemistry Chemical Physics*, 2014, **16**, 4720-4727.
7.  Y. Li and Q. Sun, *Advanced Energy Materials*, 2016, **6**, 1600463.

8.      H. Xie, T. Wang, J. Liang, Q. Li and S. Sun, *Nano Today*, 2018, **21**, 41-54.
9.      M. B. Gawande, A. Goswami, F.-X. Felpin, T. Asefa, X. Huang, R. Silva, X. Zou, R. Zboril and R. S. Varma, *Chemical Reviews*, 2016, **116**, 3722-3811.
10.     Z. Gu, H. Shen, L. Shang, X. Lv, L. Qian and G. Zheng, *Small Methods*, 2018, **2**, 1800121.
11.     S. Nitopi, E. Bertheussen, S. B. Scott, X. Liu, A. K. Engstfeld, S. Horch, B. Seger, I. E. L. Stephens, K. Chan, C. Hahn, J. K. Nørskov, T. F. Jaramillo and I. Chorkendorff, *Chemical Reviews*, 2019, **119**, 7610-7672.
12.     J. Zhao, S. Xue, J. Barber, Y. Zhou, J. Meng and X. Ke, *Journal of Materials Chemistry A*, 2020, **8**, 4700-4734.
13.     D. Gao, R. M. Arán-Ais, H. S. Jeon and B. Roldan Cuenya, *Nature Catalysis*, 2019, **2**, 198-210.
14.     L. Fan, C. Xia, F. Yang, J. Wang, H. Wang and Y. Lu, *Science Advances*, 2020, **6**, eaay3111.
15.     X. Zhao, L. Du, B. You and Y. Sun, *Catalysis Science & Technology*, 2020, **10**, 2711-2720.
16.     K. Jiang, R. B. Sandberg, A. J. Akey, X. Liu, D. C. Bell, J. K. Nørskov, K. Chan and H. Wang, *Nature Catalysis*, 2018, **1**, 111-119.
17.     T. Cheng, H. Xiao and W. A. Goddard, *Journal of the American Chemical Society*, 2016, **138**, 13802-13805.
18.     I. V. Chernyshova, P. Somasundaran and S. Ponnurangam, *Proceedings of the National Academy of Sciences*, 2018, **115**, E9261.
19.     P. G. Russell, N. Kovac, S. Srinivasan and M. Steinberg, *Journal of The Electrochemical Society*, 1977, **124**, 1329-1338.
20.     S. Kapusta and N. Hackerman, *Journal of The Electrochemical Society*, 1983, **130**, 607-613.
21.     R. L. Cook, R. C. MacDuff and A. F. Sammells, *Journal of The Electrochemical Society*, 1989, **136**, 1982-1984.
22.     Y. Hori, A. Murata and R. Takahashi, *Journal of the Chemical Society, Faraday Transactions 1: Physical Chemistry in Condensed Phases*, 1989, **85**, 2309-2326.
23.     Y. Hori, A. Murata, R. Takahashi and S. Suzuki, *Journal of the American Chemical Society*, 1987, **109**, 5022-5023.
24.     F. Calle-Vallejo and M. T. M. Koper, *ACS Catalysis*, 2017, **7**, 7346-7351.
25.     A. A. Peterson, F. Abild-Pedersen, F. Studt, J. Rossmeisl and J. K. Nørskov, *Energy & Environmental Science*, 2010, **3**, 1311-1315.
26.     I. T. Y. Hori, O. Koga, N. Hoshi, *Journal of Molecular Catalysis A: Chemical* 2003, **199**, 39-47.
27.     J. H. Montoya, C. Shi, K. Chan and J. K. Nørskov, *The Journal of Physical Chemistry Letters*, 2015, **6**, 2032-2037.
28.     A. J. Garza, A. T. Bell and M. Head-Gordon, *ACS Catalysis*, 2018, **8**, 1490-1499.
29.     J. D. Goodpaster, A. T. Bell and M. Head-Gordon, *The Journal of Physical Chemistry Letters*, 2016, **7**, 1471-1477.
30.     T. K. Todorova, M. W. Schreiber and M. Fontecave, *ACS Catalysis*, 2020, **10**, 1754-1768.
31.     H. Xiao, T. Cheng and W. A. Goddard, *Journal of the American Chemical Society*, 2017, **139**, 130-136.
32.     T. Cheng, H. Xiao and W. A. Goddard, *Proceedings of the National Academy of Sciences*, 2017, **114**, 1795.
33.     W. Luo, X. Nie, M. J. Janik and A. Asthagiri, *ACS Catalysis*, 2016, **6**, 219-229.
34.     F. Calle-Vallejo and M. T. M. Koper, *Angewandte Chemie International Edition*, 2013, **52**, 7282-7285.
35.     S. Hanselman, M. T. M. Koper and F. Calle-Vallejo, *ACS Energy Letters*, 2018, **3**, 1062-1067.
36.     K. P. Kuhl, E. R. Cave, D. N. Abram and T. F. Jaramillo, *Energy & Environmental Science*, 2012, **5**, 7050-7059.
37.     J. Resasco, L. D. Chen, E. Clark, C. Tsai, C. Hahn, T. F. Jaramillo, K. Chan and A. T. Bell, *Journal of the American Chemical Society*, 2017, **139**, 11277-11287.
38.     K. J. P. Schouten, Y. Kwon, C. J. M. van der Ham, Z. Qin and M. T. M. Koper, *Chemical Science*, 2011, **2**, 1902-1909.

39. I. Ledezma-Yanez, E. P. Gallent, M. T. M. Koper and F. Calle-Vallejo, *Catalysis Today*, 2016, **262**, 90-94.

40. K. J. P. Schouten, Z. Qin, E. Pérez Gallent and M. T. M. Koper, *Journal of the American Chemical Society*, 2012, **134**, 9864-9867.

41. C. Hahn, T. Hatsukade, Y.-G. Kim, A. Vailionis, J. H. Baricuatro, D. C. Higgins, S. A. Nitopi, M. P. Soriaga and T. F. Jaramillo, *Proceedings of the National Academy of Sciences*, 2017, **114**, 5918.

42. F. S. Roberts, K. P. Kuhl and A. Nilsson, *ChemCatChem*, 2016, **8**, 1119-1124.

43. G. Mangione, J. Huang, R. Buonsanti and C. Corminboeuf, *The Journal of Physical Chemistry Letters*, 2019, **10**, 4259-4265.

44. A. Loiudice, P. Lobaccaro, E. A. Kamali, T. Thao, B. H. Huang, J. W. Ager and R. Buonsanti, *Angewandte Chemie*, 2016, **128**, 5883-5886.

45. G. L. De Gregorio, T. Burdyny, A. Loiudice, P. Iyengar, W. A. Smith and R. Buonsanti, *ACS Catalysis*, 2020, **10**, 4854-4862.

46. Y. Wang, Z. Wang, C.-T. Dinh, J. Li, A. Ozden, M. Golam Kibria, A. Seifitokaldani, C.-S. Tan, C. M. Gabardo, M. Luo, H. Zhou, F. Li, Y. Lum, C. McCallum, Y. Xu, M. Liu, A. Proppe, A. Johnston, P. Todorovic, T.-T. Zhuang, D. Sinton, S. O. Kelley and E. H. Sargent, *Nature Catalysis*, 2020, **3**, 98-106.

47. X. Feng, K. Jiang, S. Fan and M. W. Kanan, *ACS Central Science*, 2016, **2**, 169-174.

48. H. Jung, S. Y. Lee, C. W. Lee, M. K. Cho, D. H. Won, C. Kim, H.-S. Oh, B. K. Min and Y. J. Hwang, *Journal of the American Chemical Society*, 2019, **141**, 4624-4633.

49. A. Verdaguer-Casadevall, C. W. Li, T. P. Johansson, S. B. Scott, J. T. McKeown, M. Kumar, I. E. L. Stephens, M. W. Kanan and I. Chorkendorff, *Journal of the American Chemical Society*, 2015, **137**, 9808-9811.

50. Z. Chen, T. Wang, B. Liu, D. Cheng, C. Hu, G. Zhang, W. Zhu, H. Wang, Z.-J. Zhao and J. Gong, *Journal of the American Chemical Society*, 2020, **142**, 6878-6883.

51. R. B. Sandberg, J. H. Montoya, K. Chan and J. K. Nørskov, *Surface Science*, 2016, **654**, 56-62.

52. K. Jiang, Y. Huang, G. Zeng, F. M. Toma, W. A. Goddard and A. T. Bell, *ACS Energy Letters*, 2020, **5**, 1206-1214.

53. L. Wang, S. Nitopi, A. B. Wong, J. L. Snider, A. C. Nielander, C. G. Morales-Guio, M. Orazov, D. C. Higgins, C. Hahn and T. F. Jaramillo, *Nature Catalysis*, 2019, **2**, 702-708.

54. M. Ma, K. Djanashvili and W. A. Smith, *Angewandte Chemie International Edition*, 2016, **55**, 6680-6684.

55. Y. C. Li, Z. Wang, T. Yuan, D.-H. Nam, M. Luo, J. Wicks, B. Chen, J. Li, F. Li, F. P. G. de Arquer, Y. Wang, C.-T. Dinh, O. Voznyy, D. Sinton and E. H. Sargent, *Journal of the American Chemical Society*, 2019, **141**, 8584-8591.

56. T. T. H. Hoang, S. Verma, S. Ma, T. T. Fister, J. Timoshenko, A. I. Frenkel, P. J. A. Kenis and A. A. Gewirth, *Journal of the American Chemical Society*, 2018, **140**, 5791-5797.

57. N. R. Kim, K. Shin, I. Jung, M. Shim and H. M. Lee, *The Journal of Physical Chemistry C*, 2014, **118**, 26324-26331.

58. S. Shen, X. Peng, L. Song, Y. Qiu, C. Li, L. Zhuo, J. He, J. Ren, X. Liu and J. Luo, *Small*, 2019, **15**, 1902229.

59. Y. Lum, T. Cheng, W. A. Goddard and J. W. Ager, *Journal of the American Chemical Society*, 2018, **140**, 9337-9340.

60. X. Su, Y. Sun, L. Jin, L. Zhang, Y. Yang, P. Kerns, B. Liu, S. Li and J. He, *Applied Catalysis B: Environmental*, 2020, **269**, 118800.

61. A. Dutta, I. Z. Montiel, R. Erni, K. Kiran, M. Rahaman, J. Drnec and P. Broekmann, *Nano Energy*, 2020, **68**, 104331.

62. Y. Lum and J. W. Ager, *Energy & Environmental Science*, 2018, **11**, 2935-2944.

63. J. Huang, M. Mensi, E. Oveisi, V. Mantella and R. Buonsanti, *Journal of the American Chemical Society*, 2019, **141**, 2490-2499.

64. C. G. Morales-Guio, E. R. Cave, S. A. Nitopi, J. T. Feaster, L. Wang, K. P. Kuhl, A. Jackson, N. C. Johnson, D. N. Abram, T. Hatsukade, C. Hahn and T. F. Jaramillo, *Nature Catalysis*, 2018, **1**, 764-771.

65. A. A. Peterson and J. K. Nørskov, *The Journal of Physical Chemistry Letters*, 2012, **3**, 251-258.

66. D. Ren, B. S.-H. Ang and B. S. Yeo, *ACS Catalysis*, 2016, **6**, 8239-8247.

67. H. Xiao, W. A. Goddard, T. Cheng and Y. Liu, *Proceedings of the National Academy of Sciences*, 2017, **114**, 6685.

68. A. Eilert, F. Cavalca, F. S. Roberts, J. Osterwalder, C. Liu, M. Favaro, E. J. Crumlin, H. Ogasawara, D. Friebel, L. G. M. Pettersson and A. Nilsson, *The Journal of Physical Chemistry Letters*, 2017, **8**, 285-290.

69. A. J. Garza, A. T. Bell and M. Head-Gordon, *The Journal of Physical Chemistry Letters*, 2018, **9**, 601-606.

70. Y. Lum and J. W. Ager, *Angewandte Chemie International Edition*, 2018, **57**, 551-554.

71. F. Cavalca, R. Ferragut, S. Aghion, A. Eilert, O. Diaz-Morales, C. Liu, A. L. Koh, T. W. Hansen, L. G. M. Pettersson and A. Nilsson, *The Journal of Physical Chemistry C*, 2017, **121**, 25003-25009.

72. T.-C. Chou, C.-C. Chang, H.-L. Yu, W.-Y. Yu, C.-L. Dong, J.-J. Velasco-Vélez, C.-H. Chuang, L.-C. Chen, J.-F. Lee, J.-M. Chen and H.-L. Wu, *Journal of the American Chemical Society*, 2020, **142**, 2857-2867.

73. C. M. Gunathunge, V. J. Ovalle, Y. Li, M. J. Janik and M. M. Waegele, *ACS Catalysis*, 2018, **8**, 7507-7516.

74. H. Mistry, A. S. Varela, C. S. Bonifacio, I. Zegkinoglou, I. Sinev, Y.-W. Choi, K. Kisslinger, E. A. Stach, J. C. Yang, P. Strasser and B. R. Cuenya, *Nature Communications*, 2016, **7**, 12123.

75. A. S. Varela, M. Kroschel, T. Reier and P. Strasser, *Catalysis Today*, 2016, **260**, 8-13.

76. D. Gao, I. Zegkinoglou, N. J. Divins, F. Scholten, I. Sinev, P. Grosse and B. Roldan Cuenya, *ACS Nano*, 2017, **11**, 4825-4831.

77. Y. Zhou, F. Che, M. Liu, C. Zou, Z. Liang, P. De Luna, H. Yuan, J. Li, Z. Wang, H. Xie, H. Li, P. Chen, E. Bladt, R. Quintero-Bermudez, T.-K. Sham, S. Bals, J. Hofkens, D. Sinton, G. Chen and E. H. Sargent, *Nature Chemistry*, 2018, **10**, 974-980.

78. Y. Huang, A. D. Handoko, P. Hirunsit and B. S. Yeo, *ACS Catalysis*, 2017, **7**, 1749-1756.

79. Q. T. Trinh, A. Banerjee, Y. Yang and S. H. Mushrif, *The Journal of Physical Chemistry C*, 2017, **121**, 1099-1112.

80. C. Chen, X. Sun, L. Lu, D. Yang, J. Ma, Q. Zhu, Q. Qian and B. Han, *Green Chemistry*, 2018, **20**, 4579-4583.

81. J. M. Luther, P. K. Jain, T. Ewers and A. P. Alivisatos, *Nature Materials*, 2011, **10**, 361-366.

82. T.-T. Zhuang, Z.-Q. Liang, A. Seifitokaldani, Y. Li, P. De Luna, T. Burdyny, F. Che, F. Meng, Y. Min, R. Quintero-Bermudez, C. T. Dinh, Y. Pang, M. Zhong, B. Zhang, J. Li, P.-N. Chen, X.-L. Zheng, H. Liang, W.-N. Ge, B.-J. Ye, D. Sinton, S.-H. Yu and E. H. Sargent, *Nature Catalysis*, 2018, **1**, 421-428.

83. R. Kortlever, J. Shen, K. J. P. Schouten, F. Calle-Vallejo and M. T. M. Koper, *The Journal of Physical Chemistry Letters*, 2015, **6**, 4073-4082.

84. W. Ma, S. Xie, T. Liu, Q. Fan, J. Ye, F. Sun, Z. Jiang, Q. Zhang, J. Cheng and Y. Wang, *Nature Catalysis*, 2020, DOI: 10.1038/s41929-020-0450-0.

85. J. H. Montoya, A. A. Peterson and J. K. Nørskov, *ChemCatChem*, 2013, **5**, 737-742.

86. W. Ma, S. Xie, X.-G. Zhang, F. Sun, J. Kang, Z. Jiang, Q. Zhang, D.-Y. Wu and Y. Wang, *Nature Communications*, 2019, **10**, 892.

87. M. Eddaoudi, J. Kim, N. Rosi, D. Vodak, J. Wachter, M. O'Keeffe and O. M. Yaghi, *Science*, 2002, **295**, 469-472.

88. F. Li, Y. C. Li, Z. Wang, J. Li, D.-H. Nam, Y. Lum, M. Luo, X. Wang, A. Ozden, S.-F. Hung, B. Chen, Y. Wang, J. Wicks, Y. Xu, Y. Li, C. M. Gabardo, C.-T. Dinh, Y. Wang, T.-T. Zhuang, D. Sinton and E. H. Sargent, *Nature Catalysis*, 2020, **3**, 75-82.

89. Y. Zhang, K. Li, M. Chen, J. Wang, J. Liu and Y. Zhang, *ACS Applied Nano Materials*, 2020, **3**, 257-263.
90. B. An, Z. Li, Y. Song, J. Zhang, L. Zeng, C. Wang and W. Lin, *Nature Catalysis*, 2019, **2**, 709-717.
91. Y. Chen, X. Mu, E. Lester and T. Wu, *Progress in Natural Science: Materials International*, 2018, **28**, 584-589.
92. Z. Weng, Y. Wu, M. Wang, J. Jiang, K. Yang, S. Huo, X.-F. Wang, Q. Ma, G. W. Brudvig, V. S. Batista, Y. Liang, Z. Feng and H. Wang, *Nature Communications*, 2018, **9**, 415.
93. D.-H. Nam, O. S. Bushuyev, J. Li, P. De Luna, A. Seifitokaldani, C.-T. Dinh, F. P. García de Arquer, Y. Wang, Z. Liang, A. H. Proppe, C. S. Tan, P. Todorović, O. Shekhah, C. M. Gabardo, J. W. Jo, J. Choi, M.-J. Choi, S.-W. Baek, J. Kim, D. Sinton, S. O. Kelley, M. Eddaoudi and E. H. Sargent, *Journal of the American Chemical Society*, 2018, **140**, 11378-11386.
94. K. Zhao, Y. Liu, X. Quan, S. Chen and H. Yu, *ACS Applied Materials & Interfaces*, 2017, **9**, 5302-5311.
95. J. Albo, M. Perfecto-Irigaray, G. Beobide and A. Irabien, *Journal of CO2 Utilization*, 2019, **33**, 157-165.
96. Y. Lum, B. Yue, P. Lobaccaro, A. T. Bell and J. W. Ager, *The Journal of Physical Chemistry C*, 2017, **121**, 14191-14203.
97. R. Kas, R. Kortlever, H. Yılmaz, M. T. M. Koper and G. Mul, *ChemElectroChem*, 2015, **2**, 354-358.
98. X. Liu, P. Schlexer, J. Xiao, Y. Ji, L. Wang, R. B. Sandberg, M. Tang, K. S. Brown, H. Peng, S. Ringe, C. Hahn, T. F. Jaramillo, J. K. Nørskov and K. Chan, *Nature Communications*, 2019, **10**, 32.
99. C. W. Li, J. Ciston and M. W. Kanan, *Nature*, 2014, **508**, 504-507.
100. L. Wang, S. A. Nitopi, E. Bertheussen, M. Orazov, C. G. Morales-Guio, X. Liu, D. C. Higgins, K. Chan, J. K. Nørskov, C. Hahn and T. F. Jaramillo, *ACS Catalysis*, 2018, **8**, 7445-7454.
101. C.-T. Dinh, T. Burdyny, M. G. Kibria, A. Seifitokaldani, C. M. Gabardo, F. P. García de Arquer, A. Kiani, J. P. Edwards, P. De Luna, O. S. Bushuyev, C. Zou, R. Quintero-Bermudez, Y. Pang, D. Sinton and E. H. Sargent, *Science*, 2018, **360**, 783.
102. Z. Han, R. Kortlever, H.-Y. Chen, J. C. Peters and T. Agapie, *ACS Central Science*, 2017, **3**, 853-859.
103. F. Li, A. Thevenon, A. Rosas-Hernández, Z. Wang, Y. Li, C. M. Gabardo, A. Ozden, C. T. Dinh, J. Li, Y. Wang, J. P. Edwards, Y. Xu, C. McCallum, L. Tao, Z.-Q. Liang, M. Luo, X. Wang, H. Li, C. P. O'Brien, C.-S. Tan, D.-H. Nam, R. Quintero-Bermudez, T.-T. Zhuang, Y. C. Li, Z. Han, R. D. Britt, D. Sinton, T. Agapie, J. C. Peters and E. H. Sargent, *Nature*, 2020, **577**, 509-513.
104. A. Thevenon, A. Rosas-Hernández, J. C. Peters and T. Agapie, *Angewandte Chemie International Edition*, 2019, **58**, 16952-16958.
105. Z. P. Jovanov, J. Ferreira de Araujo, S. Li and P. Strasser, *The Journal of Physical Chemistry C*, 2019, **123**, 2165-2174.
106. M. R. Singh, Y. Kwon, Y. Lum, J. W. Ager and A. T. Bell, *Journal of the American Chemical Society*, 2016, **138**, 13006-13012.
107. T. Cheng, H. Xiao and W. A. Goddard, *The Journal of Physical Chemistry Letters*, 2015, **6**, 4767-4773.

**Table 1:** Electrochemical $CO_2$ reduction reactions with equilibrium potentials [15].

| Half reactions | $E^0$ (V) vs. RHE at pH 7 |
| --- | --- |
| $CO_2 + e^- \rightarrow CO_2^-$ | -1.48 |
| $CO_2 + 2H^+ + 2e^- \rightarrow HCOOH(l)$ | -0.12 |
| $CO_2 + 2H^+ + 2e^- \rightarrow CO(g) + H_2O$ | -0.10 |
| $CO_2 + 6H^+ + 6e^- \rightarrow CH_3OH(l) + H_2O$ | 0.03 |
| $CO_2 + 8H^+ + 8e^- \rightarrow CH_4(g) + 2H_2O$ | 0.17 |
| $2CO_2 + 12H^+ + 12e^- \rightarrow C_2H_4(g) + 4H_2O$ | 0.08 |
| $2CO_2 + 14H^+ + 14e^- \rightarrow C_2H_5OH(l) + 3H_2O$ | 0.09 |
| $2CO_2 + 14H^+ + 14e^- \rightarrow C_2H_6(g) + 4H_2O$ | 0.14 |
| $3CO_2 + 18H^+ + 18e^- \rightarrow C_3H_7OH(l) + 5H_2O$ | 0.10 |

***Figure 1:*** *Possible reaction pathways for $CO_2$ reduction to C1-products where the colors represent pathways suggested by different research groups: blue – ref [83], red – ref [3, 98], and green – ref [107]. Colored arrows are used to indicate the reaction step unique to that color.*
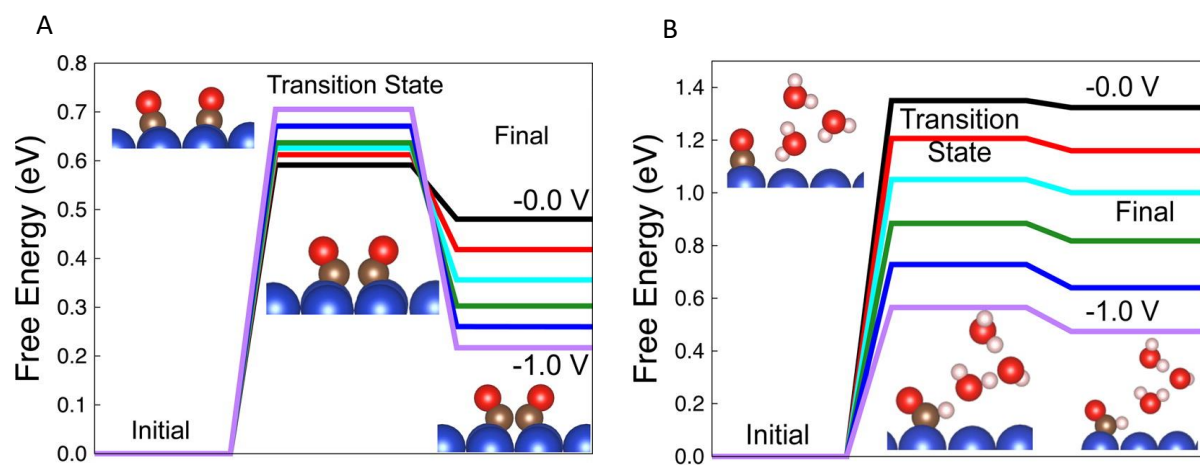
**Figure 2:** Relative free energy of the initial configuration, transition state, and final configuration for (A) *CO dimerization and (B) *CHO through the Heyrovsky mechanism. Reprinted with permission from ref [29] Copyright 2016 American Chemical Society.
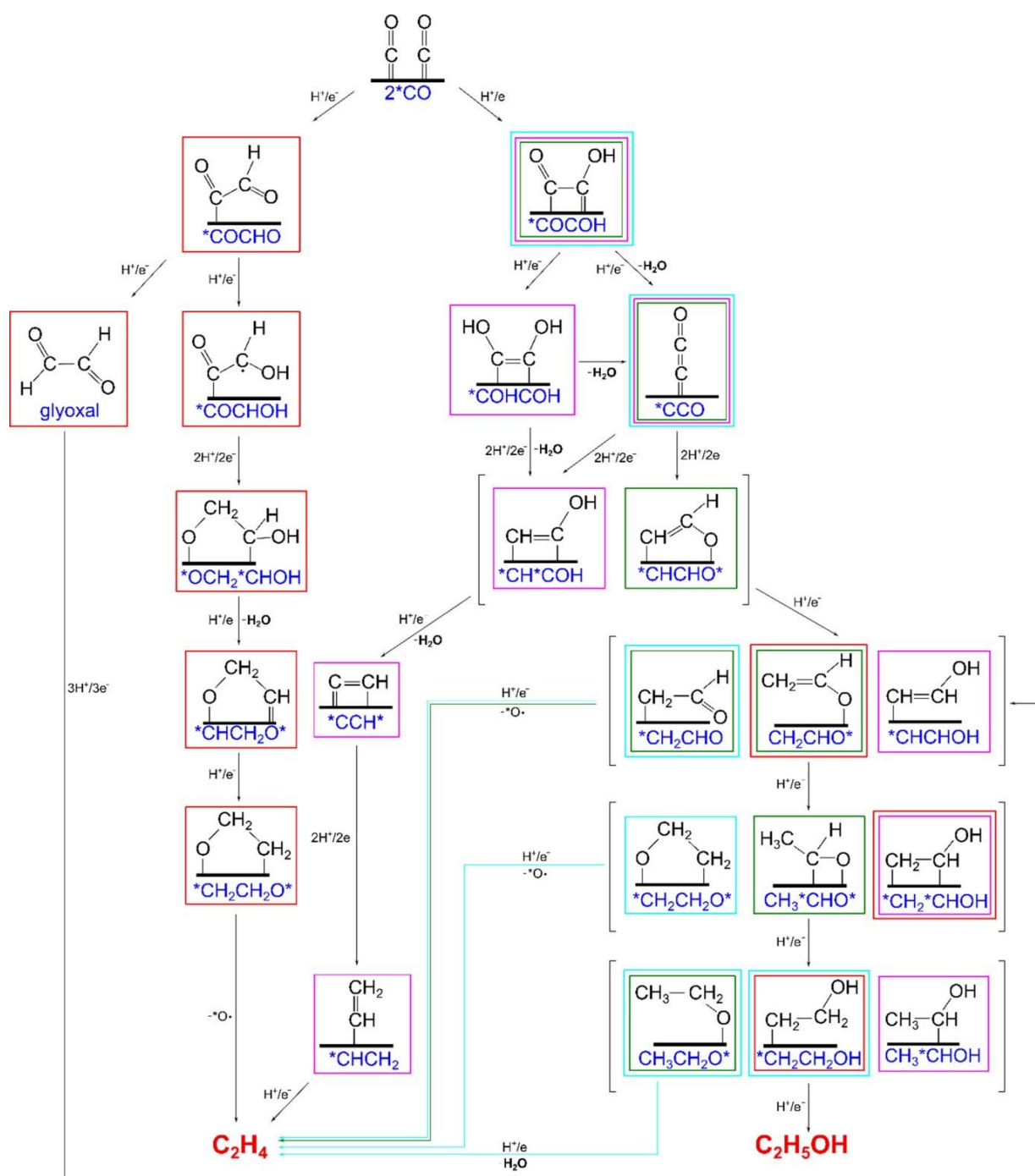
**Figure 3:** Possible mechanistic pathways of $CO_2$ reduction to $C_2H_4$ and $C_2H_5OH$ based on the work of Bell and Head-Gordon (red) [28], Goddard et.al (pink) [31, 32], Janik and Asthagiri (blue) [33], and Calle-Vallejo and Koper (green) [34, 35], with brackets encompassing different tautomers of the intermediates. Reprinted with permission from ref [30] Copyright 2020 American Chemical Society.

**Table 2:** Summary of the various catalysts discussed in this review.

| Strategy | Type of catalyst | Electrolyte | Cell design | Current density | Major product(s) | FE |
|---|---|---|---|---|---|---|
| **Facet Engineering and grain boundaries** | Cu (100) nanocubes [45] | 1M KOH | Flow cell | 300 mA/cm$^2$ | $C_2H_4$ | 57% |
| | Cu (100) nanoparticles/dendrites [46] | 7M KOH | Flow cell | $J_{c2+}$= 520 mA/cm$^2$ | $C_2H_4$ | 70% |
| | Fragmented $Cu_2O$ nanoparticles [48] | 0.1M KHCO$_3$ | H-cell | ~17.5 mA/cm$^2$ | $C_2H_4$ | 57.3% |
| | Grain boundary rich Cu [50] | 1M KOH | Flow cell | 96.62 mA/cm$^2$ | $C_2H_4$ and $C_2H_5OH$ | 70% |
| **Metallic tandem catalysts and alloys** | $Ag_{0.14}/Cu_{0.86}$ alloy [55] | 1M KOH | Flow cell | 250 mA/cm$^2$ | $C_2H_5OH$ | 41% |
| | Ag-Cu nanowire [56] | 1M KOH | Flow cell | ~300 mA/cm$^2$ | $C_2H_4$ and $C_2H_5OH$ | 60% and 25% |
| | Au-Cu alloy nanoparticles at Cu microcone array [58] | 0.5M KHCO$_3$ | H-cell | 4.9 mA/cm$^2$ | $C_2H_5OH$ | 29% |
| | $Cu_5Zn_8$ alloy [60] | 0.1M KHCO$_3$ | H-cell | 4.81 mA/cm$^2$ | $C_2H_5OH$ | 46.6% |
| | Bimetallic $Ag_{15}Cu_{85}$ [61] | 0.5M KHCO$_3$ | H-cell | ~26.3 mA/cm$^2$ | $C_2H_5OH$ | 33.7% |
| | Bimetallic $Cu_4Zn$ [66] | 0.1M KHCO$_3$ | H-cell | ~28.2 mA/cm$^2$ | $C_2H_5OH$ | 29.1% |
| **Influence of oxidation agent** | $O_2$ plasma treated Cu [74] | 0.1M KHCO$_3$ | H-cell | ~20 mA/cm$^2$ | $C_2H_4$ | 60% |
| | Boron doped Cu [77] | 0.1M KCl | H-cell | 70 mA/cm$^2$ | $C_2H_4$ and $C_2H_5OH$ | 52% and 27% |
| | Boron doped OD-derived Cu [80] | 0.1M KHCO$_3$ | H-cell | 33.4 mA/cm$^2$ | $C_2H_4$, $C_2H_5OH$ and $C_2H_6$ | 48.2% |
| | Cu(0)-Cu2S core-shell nanoparticles [82] | 1M KOH | Flow cell | ~393.75 mA/cm$^2$ | $C_{2+}$ alcohols | ~32% |
| | Fluorine-modified Cu [84] | 0.75M KOH | Flow cell | 1.6 A/cm$^2$ | $C_2H_4$ | 65% |
| **Metal organic frameworks** | Cu/Cu2O nanoparticles supported on vertically ZIF-L-coated nitrogen-doped graphene nanosheets [89] | 0.5M KHCO$_3$ | H-cell | 10.4 mA/cm$^2$ | $C_2H_5OH$ | 70.52% |
| | metal–organic framework (MOF)-regulated Cu cluster [93] | 1M KOH | Flow cell | 262 mA/cm$^2$ | $C_2H_4$ | 45% |
| | OD-Cu/C derived from HKUST-1 [94] | 0.1M KHCO$_3$ | H-cell | 1 mA/cm$^2$ | $C_2H_5OH$ | 34.8% |
| | Cu/Bi metal-organic framework [95] | 0.5M KHCO$_3$ | Flow cell | 20 mA/cm$^2$ | $C_2H_5OH$ | 28.3% |
| **Electrolyte and process conditions** | Cu in high concentrations of KOH [101] | 10M KOH | Flow cell | 275 mA/cm$^2$ | $C_2H_4$ | 66% |
| | Polycrystalline Cu with N-substituted pyridinium additives [102] | 0.1M KHCO$_3$ | Flow cell | 1.1 mA/cm$^2$ | $C_2H_4$, $C_2H_5OH$ and $C_3H_7OH$ | 33.6%, 27.1% and 11.8% |
| | N-aryl-dihydropyridinium- based oligomer with Cu layer [103] | 0.1M KHCO$_3$ | Flow cell | 230 mA/cm$^2$ | $C_2H_4$ | 72% |
| | Polycrystalline Cu with N,N'-ethylene-phenanthrolinium dibromide as molecular additive [104] | 0.1M KHCO$_3$ | Flow cell | 3.8 mA/cm$^2$ | $C_2H_4$ and $C_2H_5OH$ | 45.4% and 14.6% |
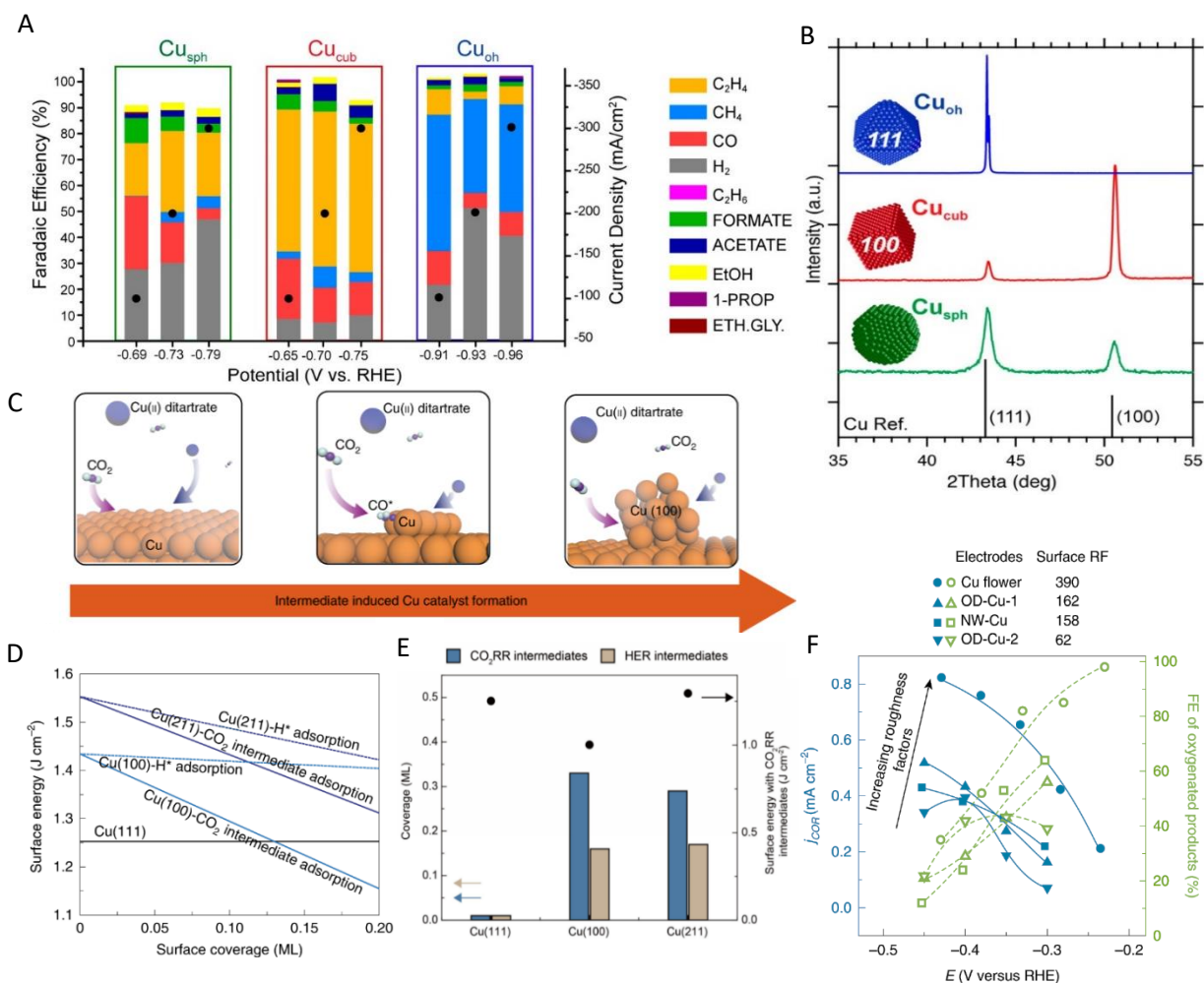
**Figure 4: Morphological and structural effects on the CO₂RR towards multicarbon products.** (A) Faradaic efficiencies as a function of potential for the Cu spheres, nanocubes, and octahedral catalysts measured in a flow cell with 1M KOH and (B) their XRD spectra. (C) Schematic illustration of how *CO acts as a capping agent to promote large fraction of Cu(100) site. (D) Surface energy as a function of surface coverage of CO₂RR and HER intermediates. (E) Calculated surface energies and intermediate coverages of the Cu(111), Cu(100), and Cu(211) facets. (F) Comparison of the geometric COR current densities and FE of oxygenated C₂₊ products for the Cu nanoflower catalyst and various state-of-the-art Cu electrodes. Figures (A)-(B) reprinted with permission from ref [45] https://pubs.acs.org/doi/10.1021/acscatal.0c00297 Copyright 2020 American Chemical Society, further permissions related to the material excerpted should be directed to the American Chemical Society. Figure (C)-(E) reprinted with permission from ref [46] Springer Nature, Nature Catalysis, Copyright 2019 and (F) reprinted with permission from ref [53], Copyright 2020 American Chemical Society.
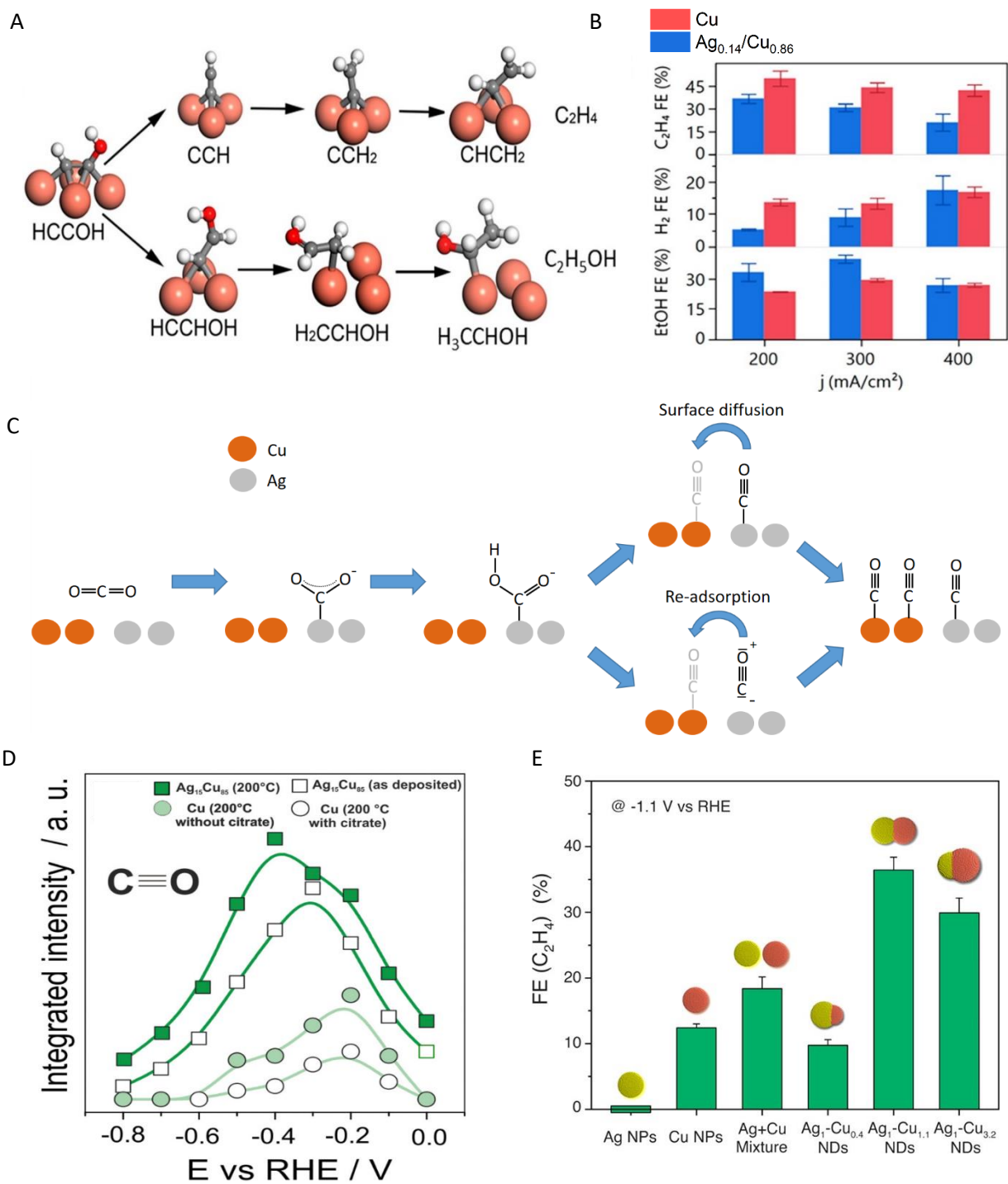
**Figure 5: The effect of Cu-based alloys and metal cocatalysts.** (A) Suggested reaction pathways for ethanol and ethylene on a Cu (111) surface. (B) FE of the bimetallic Ag/Cu catalyst compared to Cu. (C) Suggested transfer mechanism of CO from Ag to Cu sites. (D) Integrated intensities of Raman peaks assigned to the intramolecular CO stretching modes. (E) Ethylene FE for various Cu and Ag nanoparticles and nanodimers. Figures reprinted with permission from: (A)-(B) ref [55] Copyright 2019 American Chemical Society, (D) ref [61] Copyright 2019 Elsevier, and (E) ref [63] Copyright 2019 American Chemical Society.
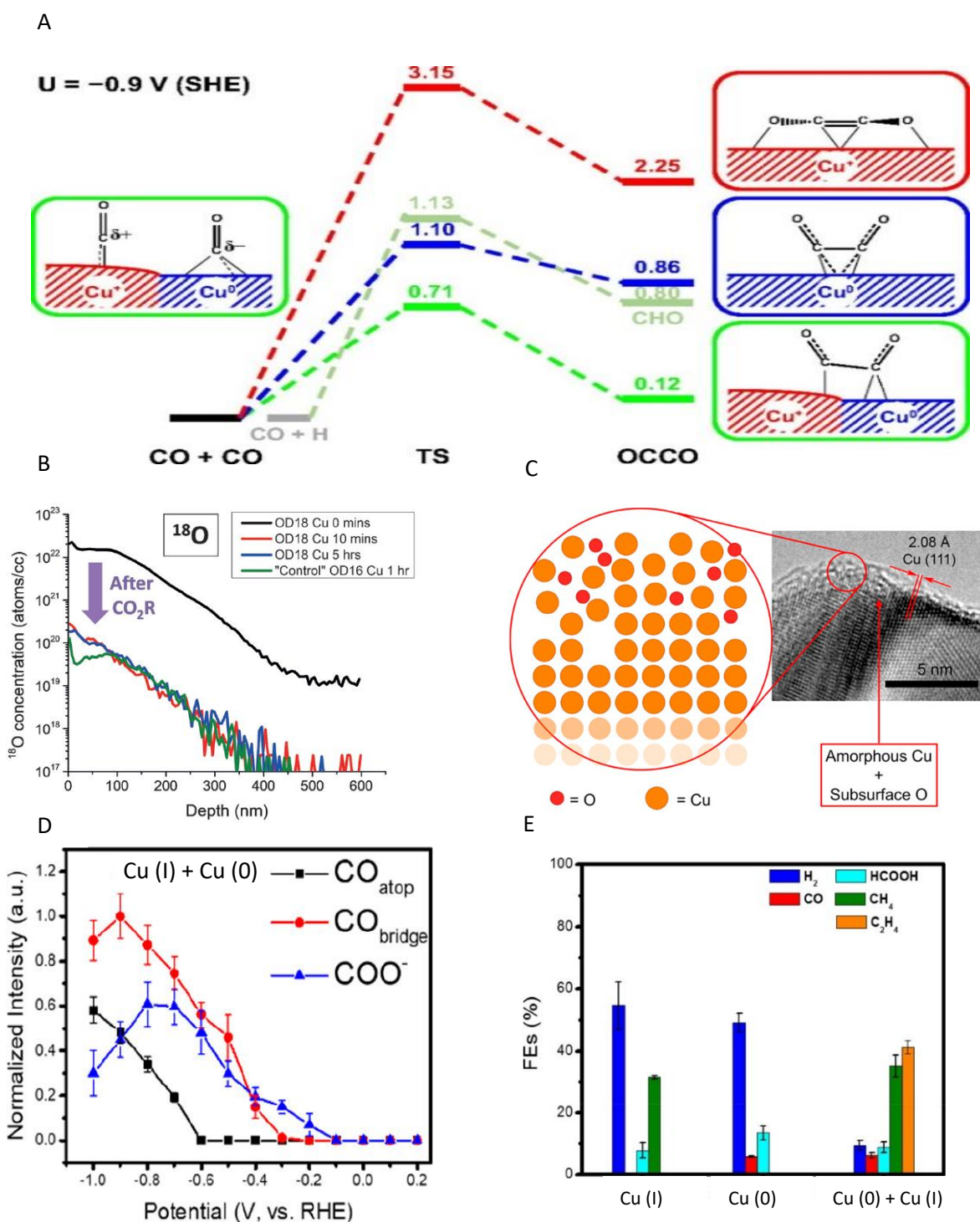
**Figure 6: Influence of oxidation state on the CO₂RR** (A) Free energy profiles for CO dimerization and CO hydrogenation for a $Cu^+$, $Cu^0$, and mixed $Cu^+$ and $Cu^0$ surface, where the initial structure for the mixed $Cu^+$ and $Cu^0$ surface is shown to the left. (B) $^{18}O$ content obtained by SIMS of OD Cu after different times of $CO_2$ reduction. (C) HRTEM with schematic illustration showing the amorphous Cu layer with subsurface oxygen. (D) Potential dependence of the intensity of atop-adsorbed CO, bridge-adsorbed CO and COO⁻ obtained by In situ SEIRAS for the catalyst with mixed $Cu^+$ and $Cu^0$ sites. (E) Selectivity of Cu catalysts containing different oxidation sites. Figures reprinted with permission from: (A) ref [67], (B) ref [70] Copyright 2018 John Wiley and Sons, and (C) ref [71] Copyright 2017 American Chemical Society. Figures (D)-(E) adapted from ref [72] Copyright 2020 American Chemical Society.
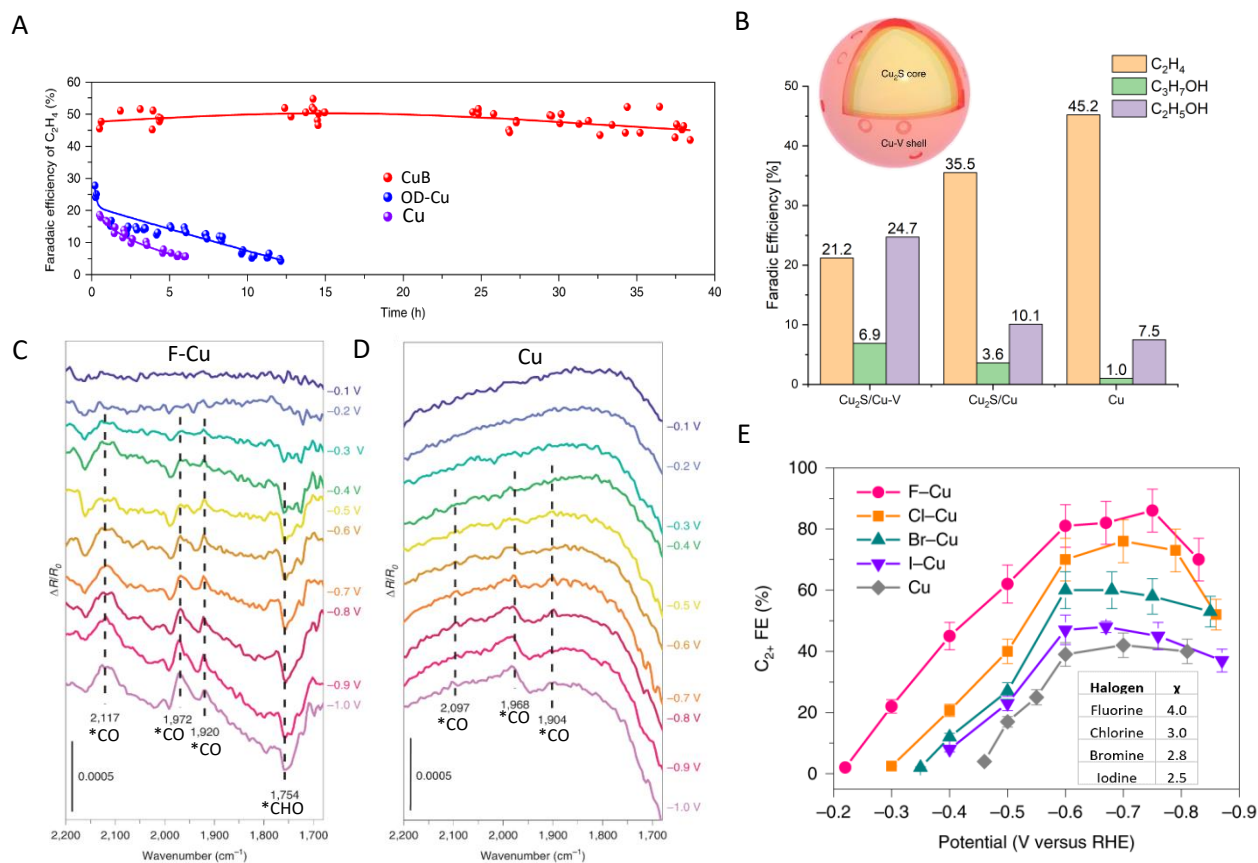
**Figure 7: Alternative oxidizers effect on the multicarbon selectivity.** (A) Faradaic efficiencies for ethylene for the CuB, OD-Cu, and Cu catalyst as a function of time at an applied potential of -1.1V vs. RHE. (B) $C_{2+}$ product selectivity of the Sulphur doped Cu catalyst with and without vacancies with the inset showing the core-shell structure, and octahedral catalysts measured in a flow cell with 1M KOH. (C) ATR-FTIRS spectra of F-Cu and (D) Cu. (E) $C_{2+}$ FE of the halogen-modified Cu catalysts with electronegativity of the halogens inset. Figures adapted with permission from: (A) ref [77] Springer Nature, Nature Catalysis, Copyright 2018, (B) ref [82] Springer Nature, Nature Catalysis, Copyright 2018, and (C)-(E) ref [84] Springer Nature, Nature Catalysis, Copyright 2020.
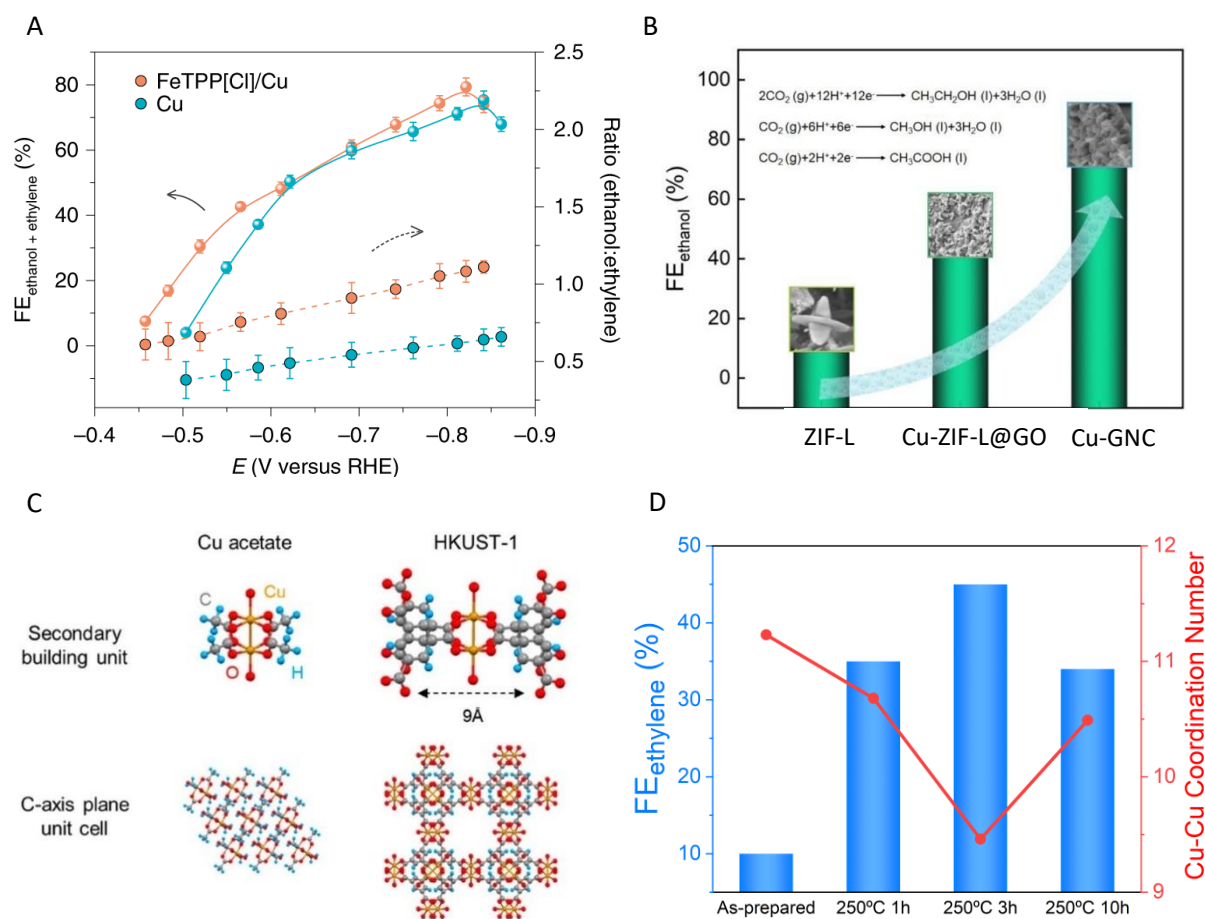
**Figure 8: Different MOF-based Cu catalysts and the effect on the C$_2$ selectivity.** (A) FE of ethylene and ethanol and the ratio of ethanol to ethylene for the FeTPP[Cl]/Cu as a function of potential. (B) Ethanol FE for the ZIF-L derived Cu catalysts. (C) Paddlewheel structure of HKUST-1 compared to the Cu acetate structure used as a reference sample. (D) Ethylene FE and Cu-Cu coordination number as a function of pretreatment conditions. Figures reprinted with permission from: (A) ref [88] Springer Nature, Nature Catalysis, Copyright 2019, and (C) ref [93] Copyright 2018 American Chemical Society. Figures adapted from (B) ref [89] Copyright 2020 American Chemical Society and (D) ref [93] Copyright 2018 American Chemical Society.
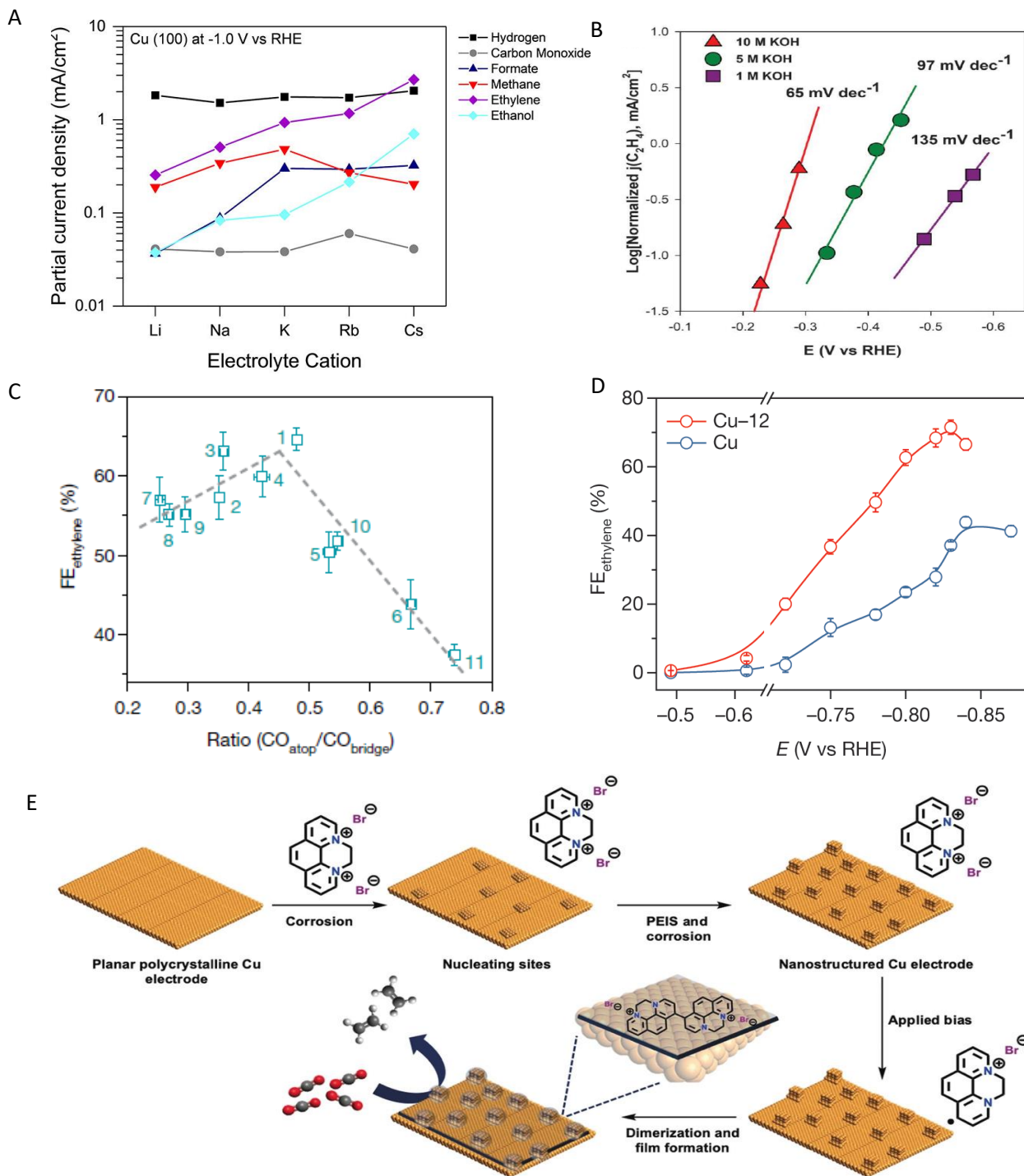
**Figure 9: Various process conditions effect on the multicarbon selectivity.** (A) Partial current densities of reaction products with different electrolyte cations over a Cu(100) oriented thin film at -1.0V vs. RHE. (B) Partial current density for ethylene and tafel slopes for different concentrations of KOH. (C) Ethylene FE as a function of the ratio of $CO_{atop}$ to $CO_{bridge}$. (D) Ethylene FE of the Cu catalyst with the N-aryl-dihydropyridine-based oligomer film (Cu-12). (E) process flow depicting the nanostructuring of the polycrystalline Cu catalyst and the subsequent electrodeposition of 1-Br. Figures reprinted with permission from: (A) ref [37] Copyright 2017 American Chemical Society, (B) ref [101] The American Association for the Advancement of Science, Science, Copyright 2018, (C)-(D) ref [103] Springer Nature, Nature Catalysis, Copyright 2019, and (E) ref [104] Copyright 2019 Wiley and Sons.